Peer-Reviewed Technical Communication

In Situ Performance Prediction of a Coherent Acoustic Modem in a Reverberant Environment

Paul A. van Walree, *Member, IEEE*, and Mathieu E. G. D. Colin

***Abstract*—A channel sounding and communications experiment was performed in the Oslofjord, using eight bottom-mounted instrument units deployed in a network configuration. Five units were equipped with a software-defined 4–8-kHz acoustic modem, programmed to transmit probe signals and communication packets in a round-robin fashion. All transmitted waveforms were recorded by all units over 35 horizontal links and 5 vertical links. The channels reveal a reverberant environment with long and dense multipath arrival patterns. Measured power-delay profiles and delay-Doppler spread functions are used to predict receiver output signal-to-noise ratio (SNR) over a signaling period of 26 h. To this end, the channel quantities are first calibrated for the propagation loss. The prediction examines the effect of ambient noise, reverberation of previously transmitted packets, the packet's own reverberation, and Doppler spread. The delay profile can be used under calm conditions, and results in a mean prediction error (averaged over all links) of about 3 dB, even hours after the measurement of the profiles. The mean error on individual links (averaged over time) is reduced to 1–2 dB by using up-to-date channel information. The relevance of predicting output SNR is finally illustrated by establishing a relationship between output SNR and the probabilities of bit and packet error.**

***Index Terms*—Acoustic communication, performance prediction, reverberation, signal fluctuations, terminology.**

I. Introduction

ADVANCES in embedded computing solutions and underwater robotics have contributed to a rapid development of underwater acoustic communications, resulting in a bewildering array of acoustic modems and modulation schemes. For the average industrial user, knowledge about the performance is limited to what is advertized by the manufacturer. However, modem performance depends strongly on the environment and cannot be captured by a few numbers in a brochure.

In the case of sonar, when the environment is known, there exist computer programs that predict the operational performance [1]. These programs take as input an environment description and sonar parameters, and their output is for instance a probability of detection as a function of target range and depth. Similarly, prediction of communication ranges or network performance could be vital for various sorts of maritime operations. The required input for a modem performance prediction tool would be an environment description, knowledge about the communication algorithms, and instrument settings like the modem source level. At the physical layer, the output would be a communication quality metric such as receiver output signal-to-noise ratio (SNR), bit error ratio (BER), or packet error ratio (PER).

Modem performance prediction can roughly be decomposed into the following three disparate subtasks:

1) acoustic channel modeling to obtain a (time-varying) channel impulse response (CIR);
2) modeling of ambient noise;
3) modeling of the physical layer to convert the CIR and the ambient noise to a communication quality metric.

Once the physical-layer model is in place, the performance prediction could be extended to the network layer. Modem performance prediction has a wider scope than channel simulation, which uses modeled or measured CIRs to develop or compare modulation schemes, for instance through channel replay [2]. Such channel simulation is based on data from past sea experiments, whereas performance prediction has to support current or near-future operational needs for specified scenarios.

Various authors have researched modem performance modeling. Ideally, the model encompasses the complete chain from environment description to communication performance, but because of the problem complexity, most authors focus on a subproblem. When the focus is on acoustic channel modeling, subtask 3) is typically replaced by convolving communication waveforms with the modeled CIR, feeding them to the receiver software to obtain the BER [3], [4]. Other authors focus on modeling of the receiver algorithms [5] or fading statistics [6], replacing subtask 1) by measured channel characteristics. Modeling the receiver performance can save much time, as intensive time-series simulations are avoided.

Stojanovic modeled the entire chain, computing upper bounds on the output SNR for several time-reversal and equalization strategies [7]. The emphasis of this article is on modeling receiver performance, as the channel was a simple time-invariant CIR with three paths derived from a shallow-water transmission geometry, combined with an assumed input SNR. Her predictions were verified by Song *et al.* [8] with experimental data, revealing excellent agreement for a time-reversal receiver. The performance of time reversal followed by a single-channel equalizer fell $\approx$ 5 dB short of the upper bound.

Siderius *et al.* used a rich set of environmental data to compute static CIRs with ray tracing [3]. Signals of an incoherent frequency-shift-keyed (FSK) modulation scheme were convolved with the modeled CIRs and demodulated by a receiver. The modeled BER was in good agreement with the BER measured at sea. Karasalo *et al.* also used ray tracing to model the acoustic channel, including Doppler shifts due to platform motion [4]. Signals of a coherent modulation scheme were

Manuscript received September 21, 2020; revised April 4, 2021; accepted May 26, 2021. Date of publication July 28, 2021; date of current version January 13, 2022. This work was supported by EDA Project Arrangement B-1467-ESM1-GP, covering the Ad Hoc Research & Technology Project titled "Smart Adaptive Long and Short Range Underwater Acoustic Networks (SALSA)." *(Corresponding author: Paul A. van Walree.)*

Associate Editor: J. Gomes.

Paul A. van Walree is with the Norwegian Defence Research Establishment (FFI), NO-3191 Horten, Norway (e-mail: paul.vanwalree@ffi.no).

Mathieu E. G. D. Colin is with the Netherlands Organisation for Applied Scientific Research (TNO), NL-2597 AK The Hague, The Netherlands (e-mail: mathieu.colin@tno.nl).

Digital Object Identifier 10.1109/JOE.2021.3085942

convolved with the modeled CIR and fed to the receiver, revealing qualitative agreement between modeled and measured BERs.

Using measured amplitude probability density functions, Yang and Yang were able to predict the BER for incoherent FSK signaling [6]. A prediction methodology for coherent signaling was developed by Preisig, through an in-depth analysis of an adaptive channel-estimate based decision-feedback equalizer and a passive time-reversal equalizer [5]. The equalizers were run in training mode, and their performance was predicted from, among other things, measured delay-Doppler spread functions. The prediction was within a few decibels of the measured performance for a calm sea, but the prediction error was larger for a rough sea surface.

Modeling of noise (subtask 2) is required for scenarios where noise affects system performance, but it is of lesser importance in reverberation-limited scenarios. Reverberation is often a limiting factor in active sonar [9], where target echoes are obscured by diffuse scattering of the detection signal from the seafloor, sea surface, and volume inhomogeneities. It typically manifests itself as a continuum of myriad arrivals. The amplitude of reverberation arrivals may be weak compared with direct or refracted paths, but their accumulated power can be nonnegligible. Practical channel equalizers are not able to unravel the resulting intersymbol interference (ISI) inflicted on modem signals, because the required filter length is prohibitive.

This article focuses on subtask 3) and develops a prediction methodology for a phase-coherent modulation scheme. The prediction uses measured delay profiles and delay-Doppler spread functions estimated from experimental data collected in the EDA-SALSA project [10]. Receiver output SNR is predicted and compared with the output SNR returned by an acoustic modem.

The contributions of this article are the following:

1) communication channel theory is linked to underwater acoustics terminology;
2) calibrated channel measurements are presented, with physical units tailored to the prediction task;
3) channel knowledge is used to predict the performance of a phase-coherent acoustic modem.

The prediction methodology is tested on a unique data set with 40 acoustic links, simultaneously monitored during 26 h in a time-varying environment. The data analysis benefits from synchronization by atomic clocks, and the results contribute to the understanding of acoustic modem performance.

The remainder of this article is organized as follows. Section II establishes a connection between communication channel quantities and underwater acoustics quantities. The time-varying impulse response and derived quantities such as the delay-Doppler spread function are calibrated for the propagation loss. The received signal power is subsequently decomposed into a useful part and an ISI part, which serve as input to various hypotheses predicting receiver output SNR, involving also ambient noise and reverberation of previous packets transmitted over the same link. Section III describes the setup and instrumentation of a sea trial in the Oslofjord, the signal-transmit schedule, the modulation scheme, and the employed channel sounders. Section IV characterizes the environment through sound-speed profiles, wind speed, and propagation loss. It also shows two long-term channel measurements, characteristic delay profiles, and illustrates the detrimental effect of reverberation on a modem signal. Prediction results are shown in Section V for 40 acoustic links, where 2 links are analyzed in detail. It is shown that receiver output SNR can be translated into probabilities of bit and packet error. Section VI discusses the findings. Finally, Section VII concludes this article.

II. Theory and Definition of Terms

A. Communications and Underwater Acoustics Terminology

In a linear time-variant channel, the acoustic field $a(t)$ at the receiver follows from the input signal $x(t)$ via the convolution integral

$$a(t) = \int_{-\infty}^{\infty} h(t,\tau)\, x(t-\tau)\, \mathrm{d}\tau + n(t) = y(t) + n(t) \tag{1}$$

where $h(t,\tau)$ is the time-varying impulse response, $y(t)$ is the distorted output signal, and $n(t)$ is ambient noise. The input and output signals can be defined to suit the application. For performance modeling of acoustic modems, it is convenient to link the quantities in (1) to underwater acoustics terminology [11]. To this end, the transmitter modem is imaginarily placed in a hypothetical, infinite uniform lossless medium. Let $x(t)$ then denote the product of range and acoustic pressure, at a distance r from the acoustic center of the modem transducer, in a specified direction in the acoustic far field

$$x(t) = rp(r,t) \tag{2}$$

and let $y(t)$ be the acoustic signal pressure at the receiver in the actual medium. The dimensions of $x(t)$, $y(t)$, and $h(t,\tau)$ become Pa m, Pa, and $\mathrm{m^{-1}s^{-1}}$, respectively. The mean-square value of $x(t)$ is known as the source factor

$$F_{\mathrm{S}} = \overline{x^2} = r^2\overline{p^2(r)} \tag{3}$$

which, using the reference values $p_0^2 = 1\ \mu\mathrm{Pa}^2$ and $r_0^2 = 1\ \mathrm{m}^2$, is related to the source level of an acoustic modem via

$$\mathrm{SL} = 10\log_{10}\left(\frac{F_{\mathrm{S}}}{p_0^2 r_0^2}\right) \quad \left[\mathrm{dB\ re\ 1\ \mu Pa^2 m^2}\right] . \tag{4}$$

The signal level is the received mean-square sound pressure level due to the signal

$$L_S = 10\log_{10}\left(\frac{\overline{y^2}}{p_0^2}\right) \quad \left[\mathrm{dB\ re\ 1\,\mu Pa^2}\right] . \tag{5}$$

The difference between the source level and the signal level is the propagation loss

$$\mathrm{PL} = \mathrm{SL} - L_S \quad \left[\mathrm{dB\ re\ 1\ m^2}\right] \tag{6}$$

$$= 10\log_{10}\left(\frac{\overline{x^2}}{r_0^2\overline{y^2}}\right) \tag{7}$$

$$= 10\log_{10}\left(\frac{F_{\mathrm{P}}^{-1}}{r_0^2}\right) \tag{8}$$

where the quantity

$$F_{\mathrm{P}} = \frac{\overline{y^2}}{\overline{x^2}} \tag{9}$$

is the propagation factor. Mean-square sound pressure is not the same as acoustic power, but the squared pressure at a location is proportional to the acoustic power per unit area at that location. To save space, the term power is used throughout this article as a synonym of mean-square sound pressure.

The remainder of this section expresses the propagation loss in terms of a time-varying CIR. Consider a scenario with wideband signaling over a time interval T in a frequency band B, where T and B denote an integration interval when used as an integral limit, or the observation period and bandwidth otherwise.

The Fourier transform of $h(t,\tau)$ with respect to τ gives the time-variant transfer function

$$H(t,f) = \int_{-\infty}^{\infty} h(t,\tau)\,\mathrm{e}^{-2\pi\mathrm{i}f\tau}\,\mathrm{d}\tau \tag{10}$$

and the Fourier transform of $x(t)$ with respect to t is

$$X(f) = \int_T x(t)\,\mathrm{e}^{-2\pi\mathrm{i}ft}\,\mathrm{d}t\ . \tag{11}$$

Substitution of the inverse Fourier transform of $X(f)$ in the superposition integral (1) yields

$$y(t) = \int_{-\infty}^{\infty} h(t,\tau)\,x(t-\tau)\,\mathrm{d}\tau \tag{12}$$

$$= \int_{-\infty}^{\infty} h(t,\tau)\,\left(\int_B X(f)\,\mathrm{e}^{2\pi\mathrm{i}f(t-\tau)}\,\mathrm{d}f\right)\,\mathrm{d}\tau \tag{13}$$

$$= \int_B X(f)\,\left(\int_{-\infty}^{\infty} h(t,\tau)\,\mathrm{e}^{-2\pi\mathrm{i}f\tau}\,\mathrm{d}\tau\right)\,\mathrm{e}^{2\pi\mathrm{i}ft}\,\mathrm{d}f \tag{14}$$

$$= \int_B X(f)H(t,f)\,\mathrm{e}^{2\pi\mathrm{i}ft}\,\mathrm{d}f\ . \tag{15}$$

In a time-invariant channel with $H(t,f) = H(f)$, the Fourier transform of (15) yields the well-known result $Y(f) = H(f)X(f)$, and

$$\int_B |Y(f)|^2\,\mathrm{d}f = \int_B |H(f)|^2\,|X(f)|^2\,\mathrm{d}f\ . \tag{16}$$

If the spectrum of the input signal is sufficiently flat over the band, this can be approximated by

$$\int_B |Y(f)|^2\,\mathrm{d}f \approx \frac{1}{B}\int_B |H(f)|^2\,\mathrm{d}f\ \int_B |X(f)|^2\,\mathrm{d}f\ . \tag{17}$$

In a time-variant channel, the reasonable assumption that input signal and impulse response are uncorrelated results in a similar expression, where $|H(f)|^2$ is replaced by the temporal mean $\overline{|H(f)|^2}$ of $|H(t,f)|^2$. The mean-square sound pressure at the receiver becomes

$$\overline{y^2} \triangleq \frac{1}{T}\int_T y^2(t)\,\mathrm{d}t \tag{18}$$

$$= \frac{1}{T}\int_B |Y(f)|^2\,\mathrm{d}f \tag{19}$$

$$\approx \left(\frac{1}{B}\int_B \overline{|H(f)|^2}\,\mathrm{d}f\right)\frac{1}{T}\int_B |X(f)|^2\,\mathrm{d}f \tag{20}$$

$$= \left(\frac{1}{B}\int_B \overline{|H(f)|^2}\,\mathrm{d}f\right)\overline{x^2} \tag{21}$$

where the steps from (18) to (19) and from (20) to (21) use Parseval's theorem.

The inverse Fourier transform

$$\tilde{h}(t,\tau) = \int_B H(t,f)\,\mathrm{e}^{2\pi\mathrm{i}f\tau}\,\mathrm{d}f \tag{22}$$

yields the band-limited impulse response $\tilde{h}(t,\tau)$,[1] and the Fourier transform of $\tilde{h}(t,\tau)$ with respect to t gives the delay-Doppler spread function $\tilde{D}(\upsilon,\tau)$ as a function of Doppler frequency shift υ and delay [12]. To arrive at simple expressions for the propagation factor later on, it is convenient to normalize this function by the square root of the product of bandwidth and observation time

$$\tilde{D}(\upsilon,\tau) \triangleq \frac{1}{\sqrt{BT}}\int_T \tilde{h}(t,\tau)\mathrm{e}^{-2\pi\mathrm{i}\upsilon t}\,\mathrm{d}t\ . \tag{23}$$

[1]Henceforth, a tilde over a symbol denotes a quantity restricted to the frequency band of the signal.

Integration of $|\tilde{D}(\upsilon,\tau)|^2$ over υ and τ yields

$$\int_{-\infty}^{\infty}\int_{-\infty}^{\infty} |\tilde{D}(\upsilon,\tau)|^2\mathrm{d}\upsilon\,\mathrm{d}\tau = \int_{-\infty}^{\infty} \tilde{P}_{\mathrm{D}}(\upsilon)\,\mathrm{d}\upsilon = \int_{-\infty}^{\infty} \tilde{P}_{\mathrm{d}}(\tau)\,\mathrm{d}\tau \tag{24}$$

where

$$\tilde{P}_{\mathrm{D}}(\upsilon) = \int_{-\infty}^{\infty} |\tilde{D}(\upsilon,\tau)|^2\mathrm{d}\tau \tag{25}$$

is the Doppler (power) spectrum, and

$$\tilde{P}_{\mathrm{d}}(\tau) = \int_{-\infty}^{\infty} |\tilde{D}(\upsilon,\tau)|^2\mathrm{d}\upsilon \tag{26}$$

is the (power) delay profile. These terms are normally associated with wide-sense stationary uncorrelated scattering (WSSUS) channels, where the integrand is the scattering function

$$\tilde{\mathcal{S}}(\upsilon,\tau) = \mathrm{E}\left[|\tilde{D}(\upsilon,\tau)|^2\right]\ . \tag{27}$$

For lack of alternative terminology, this article uses the terms Doppler spectrum and delay profile for channels that are not necessarily WSSUS. The difference is just the use of a deterministic characterization of the delay-Doppler spread, instead of a stochastic one.

Application of Parseval's theorem to (23) yields an alternative formulation of the delay profile

$$\tilde{P}_{\mathrm{d}}(\tau) = \frac{1}{BT}\int_T |\tilde{h}(t,\tau)|^2\,\mathrm{d}t \tag{28}$$

so that

$$\int_{-\infty}^{\infty} \tilde{P}_{\mathrm{d}}(\tau)\,\mathrm{d}\tau = \frac{1}{BT}\int_{-\infty}^{\infty}\int_T |\tilde{h}(t,\tau)|^2\,\mathrm{d}t\,\mathrm{d}\tau \tag{29}$$

$$= \frac{1}{BT}\int_T\int_B |H(t,f)|^2\,\mathrm{d}f\,\mathrm{d}t \tag{30}$$

$$= \frac{1}{B}\int_B \overline{|H(f)|^2}\,\mathrm{d}f\ . \tag{31}$$

Combining (9), (21), (24), and (31), the following alternative expressions emerge for the propagation factor:

$$F_{\mathrm{P}} \triangleq \frac{\overline{y^2}}{\overline{x^2}} \tag{32}$$

$$\approx \frac{1}{B}\int_B \overline{|H(f)|^2}\,\mathrm{d}f \tag{33}$$

$$= \int_{-\infty}^{\infty} \tilde{P}_{\mathrm{d}}(\tau)\,\mathrm{d}\tau \tag{34}$$

$$= \int_{-\infty}^{\infty} \tilde{P}_{\mathrm{D}}(\upsilon)\,\mathrm{d}\upsilon \tag{35}$$

$$= \int_{-\infty}^{\infty}\int_{-\infty}^{\infty} |\tilde{D}(\upsilon,\tau)|^2\,\mathrm{d}\upsilon\,\mathrm{d}\tau\ . \tag{36}$$

The propagation loss follows from (8), and the mean-square sound pressure at the receiver due to the signal follows from (3) and (9) as

$$S = F_{\mathrm{S}}F_{\mathrm{P}}\ . \tag{37}$$

Table I gives the physical units consistent with the underwater acoustics terminology of ISO 18405 [11].

The introduction of the band-limited impulse response (22) may seem odd, but this is precisely what is measured by the channel sounders of Section III-E. These sounders use a filter matched to chirp signals with a close-to-rectangular spectrum. This yields a channel estimate where each path has significant sidelobes in delay. Such sidelobes

TABLE I
PHYSICAL UNITS OF CHANNEL CHARACTERIZATION QUANTITIES

Quantity	Symbol	Units
Input signal	x	$\mathrm{Pa\,m}$
Output signal	y	Pa
Impulse response	h	$\mathrm{m^{-1}s^{-1}}$
Transfer function	H	$\mathrm{m^{-1}}$
Delay-Doppler spread function	D	$\mathrm{m^{-1}Hz^{-1/2}s^{-1/2}}$
Scattering function	$\mathcal{S}$	$\mathrm{m^{-2}Hz^{-1}s^{-1}}$
Doppler power spectrum	P_D	$\mathrm{m^{-2}Hz^{-1}}$
Power delay profile	P_d	$\mathrm{m^{-2}s^{-1}}$

are often undesirable in sonar applications, where they can obscure features of interest, but for the current application they are desirable and important. These sidelobes preserve a maximum of channel information over the band, including the frequency dependence of the propagation loss. This information is compromised by tapering the chirps, and it is completely absent from narrowband channel models that represent each propagation path by a Dirac delta function, or a single tap in a discrete-time implementation. For (33)–(36) to hold, it is important that the frequency band of the CIR match the band of the input signal.

B. Performance Prediction

The key ingredient of the performance prediction is to split (34) and (36) into a useful part and an ISI part, which can be multiplied by F_S (37) to yield the signal power that can be harvested, and the signal power that acts as self-interference. A channel equalizer is at best able to utilize the power from the multipath arrivals within its reach. Paths at delays where the equalizer has no taps will act as interference.

The receiver of Section III-C centers the strongest path in a feedforward filter of length $\Delta\tau$. If the equalizer manages to utilize all arrivals within its filter span, the useful power is

$$S_\mathrm{U} = F_\mathrm{S} \int_{\tau_0-\Delta\tau/2}^{\tau_0+\Delta\tau/2} \tilde{P}_\mathrm{d}(\tau)\,\mathrm{d}\tau \tag{38}$$

and the self-interference is

$$S_\mathrm{ISI} = F_\mathrm{S} \left(\int_{-\infty}^{\tau_0-\Delta\tau/2} \tilde{P}_\mathrm{d}(\tau)\,\mathrm{d}\tau + \int_{\tau_0+\Delta\tau/2}^{\infty} \tilde{P}_\mathrm{d}(\tau)\,\mathrm{d}\tau \right) \tag{39}$$

with $S_\mathrm{U} + S_\mathrm{ISI} = S$, and

$$\tau_0 = \arg\max_\tau \tilde{P}_\mathrm{d}(\tau)\ . \tag{40}$$

In dynamic channels with a large Doppler spread, the receiver may not be able to harvest all power within its span, as it cannot update its filter coefficients fast enough to track the channel fluctuations. It is hypothesized that the useful and ISI parts can now be represented by

$$S_\mathrm{U} = F_\mathrm{S} \int_{\tau_0-\Delta\tau/2}^{\tau_0+\Delta\tau/2} \int_{\upsilon_0-\Delta\upsilon}^{\upsilon_0+\Delta\upsilon} |\tilde{D}(\upsilon,\tau)|^2\,\mathrm{d}\upsilon\,\mathrm{d}\tau \tag{41}$$

and

$$S_\mathrm{ISI} = F_\mathrm{S} \int_{-\infty}^{\infty} \int_{-\infty}^{\infty} |\tilde{D}(\upsilon,\tau)|^2\,\mathrm{d}\upsilon\,\mathrm{d}\tau - S_\mathrm{U} \tag{42}$$

respectively, where $\Delta\upsilon$ is the largest Doppler frequency shift that can be handled by the adaptive filter. For $\Delta\upsilon = \infty$, (41) and (42) are equal to (38) and (39). The computation assumes that the receiver synchronizes on the peak value of the delay-Doppler spread function

$$\upsilon_0, \tau_0 = \arg\max_{\upsilon,\tau} |\tilde{D}(\upsilon,\tau)|^2 \tag{43}$$

yielding simultaneous time and Doppler synchronization. Synchronization in the Doppler domain is possible because the receiver uses a Doppler filter bank for preamble detection.

If $\tilde{D}(\upsilon,\tau)$ were known there would be no need for (38) and (39), as they are contained in (41) and (42). Nonetheless there is a place for (38) and (39) in the analysis, because $\tilde{P}_\mathrm{d}(\tau)$ is easier to measure than $\tilde{D}(\upsilon,\tau)$. Section V shows that a prediction based on the delay profile yields excellent results under calm conditions.

The ambient noise power is defined as the in-band mean-square sound pressure at the receiver in the absence of modem transmissions, i.e.,

$$N = \overline{\tilde{n}^2}\ . \tag{44}$$

In a networking scenario, there can be transmissions of other modems that interfere with the reception of the intended modem signal. This is known as a collision. When the channel delay spread is large, it is also possible that successive transmissions over the same link collide. This is the case in the present experiment, where packet $x(t)$ was sent before the reverberation $y'(t)$ of a previous packet $x'(t)$ had died out, resulting in a "soft" collision. The received power of the colliding packet can be written as

$$C = \overline{y'^2}\ . \tag{45}$$

The last ingredient of the performance prediction is the processing gain for communication packets whose symbols are spread over K subbands (see Section III-C). The theoretical spread-spectrum gain is K if the subband signals add coherently in the processing, and the subband noise incoherently. This condition is met in an additive white Gaussian noise (AWGN) channel, and the analysis in Section V-G shows that the experimentally observed gain is close to K.

Four hypotheses are tested to predict the output SNR of the intended packet. The first hypothesis assumes a perfect receiver that is able to harvest all signal power. The ratio of signal power to noise power at the output of the receiver then equals the ratio at the input of the receiver, augmented with the processing gain. The output SNR is K times the input SNR

$$\mathrm{SNR} = \frac{KS}{N} = \frac{K(S_\mathrm{U} + S_\mathrm{ISI})}{N}\ . \tag{46}$$

The second hypothesis recognizes the possibility of a collision, where the interfering packet adds to the effective noise background. This yields a prediction based on the signal-to-background ratio (SBR)

$$\mathrm{SBR} = \frac{K(S_\mathrm{U} + S_\mathrm{ISI})}{C + N}\ . \tag{47}$$

The third hypothesis assumes that noise and collisions are not important at all, and that the system is instead limited by the packet's own interference

$$\mathrm{SIR} = \frac{KS_\mathrm{U}}{S_\mathrm{ISI}}\ . \tag{48}$$

This is the signal-to-interference ratio (SIR) hypothesis, where the signal in this case is the useful part, and the interference is the ISI part of the received signal power. The final hypothesis assumes that everything is important

$$\mathrm{SIBR} = \frac{KS_\mathrm{U}}{S_\mathrm{ISI} + C + N} \tag{49}$$

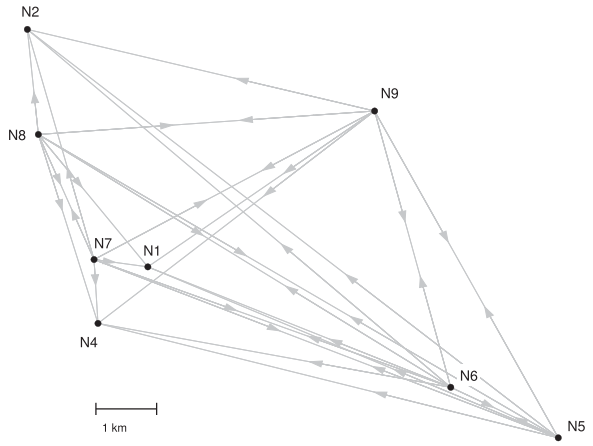

Fig. 1. Deployment topology with traffic directions.

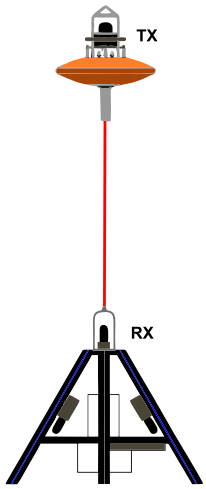

Fig. 2. NILUS bottom node with software-defined modem. Note that the length of the cable between transmitter and receiver is not to scale. The receiver is 1 m above the seafloor, the transmitter 6 m.

yielding a prediction based on the signal-to-interference-plus-background ratio (SIBR).

This terminology is potentially confusing, since collisions are often referred to as interference in the communications networking literature, and since the sonar literature often uses the term background for the detection signal's own reverberation plus noise. For lack of a better solution, this article reserves the term interference for the signal's self-interference. The interference by other packets is referred to as a collision, or as background in combination with noise.

The SNR hypothesis (46) is the theoretical upper performance bound, because it assumes perfect utilization of all signal power. A receiver cannot do better than that. However, the SIBR prediction (49) is the practical upper bound within the simple framework of this theory. The reason for testing the other hypotheses is to examine the relative importance of noise, collisions, and self-interference.

III. Experiment Description

A. Area and Node Geometry

The SALSA channel soundings and communications trial was conducted in the Oslofjord in Norway, from April 30 to May 2, 2019. Eight Networked InteLligent Underwater Sensors (NILUS) bottom nodes were deployed in the network configuration of Fig. 1. NILUS has a tripod frame with one hydrophone on the top and three hydrophones on the inside of the legs, as depicted in Fig. 2. Five units were equipped with a software-defined modem, whose transmitter hovers 5 m above the frame by the buoyancy of a disk-shaped float [13]. Since the default modem receiver is the hydrophone on top of the tripod, there is a vertical separation of 5 m between transmitter and receiver.

Table II gives bottom depths and other node characteristics. The NILUS units have a serial number that is used to abbreviate, for instance, NILUS 1 by N1, etc. The shortest transmission range is 0.89 km between N7 and N1, and the longest range is 11.0 km between N5 and N2.

The trial area has rugged terrain. A high-resolution bathymetry map was used in the planning stage to select node positions on sea mounts and ridges, but unfortunately N6 missed the top of the hill during deployment. Its transmitter had a line of sight to the receivers of N7 and N8, but its receiver was shadowed by the hill for the transmitters of N7 and N8. Apart from N7→N6 and N8→N6, all links had an existing line of sight.

TABLE II
Summary of Node Characteristics: Bottom Depth, Transmit Capability (4–8-kHz Band), Receive Capability, Clock Accuracy, and Source Level for LFM Probe Signals and Comms Packets in dB re 1 μPa^{2}m^2

Node	Depth	Tx	Rx	Atomic clock	SL LFM	SL comms
N1	55 m	n	y	y		
N2	74 m	n	y	y		
N4	89 m	n	y	n		
N5	57 m	y	y	y	185	180
N6	69 m	y	y	y	185	180
N7	37 m	y	y	y	185	180
N8	21 m	y	y	y	185	180
N9	15 m	y	y	y	185	180

NB. N3 is an existing unit, but was not deployed.

There are $M = 8$ bottom nodes, of which $M_{\mathrm{tr}} = 5$ transmit–receive nodes and $M_{\mathrm{r}} = 3$ receive-only units. This results in signaling over

$$\frac{M(M-1)}{2} - \frac{M_{\mathrm{r}}(M_{\mathrm{r}}-1)}{2} = 25 \tag{50}$$

links, of which

$$\frac{M_{\mathrm{tr}}(M_{\mathrm{tr}}-1)}{2} = 10 \tag{51}$$

links are bidirectional. Owing to the bistatic hardware configuration of the modems, and the different deployments depths of the nodes, the CIR from node A to node B is not the same as the CIR from B to A. A simple illustration is the existing line of sight for N6→N7 and N6→N8, and its absence for N8→N6 and N7→N6. This implies that there are

$$M_{\mathrm{tr}}(M_{\mathrm{tr}}-1) + M_{\mathrm{r}}M_{\mathrm{tr}} = 35 \tag{52}$$

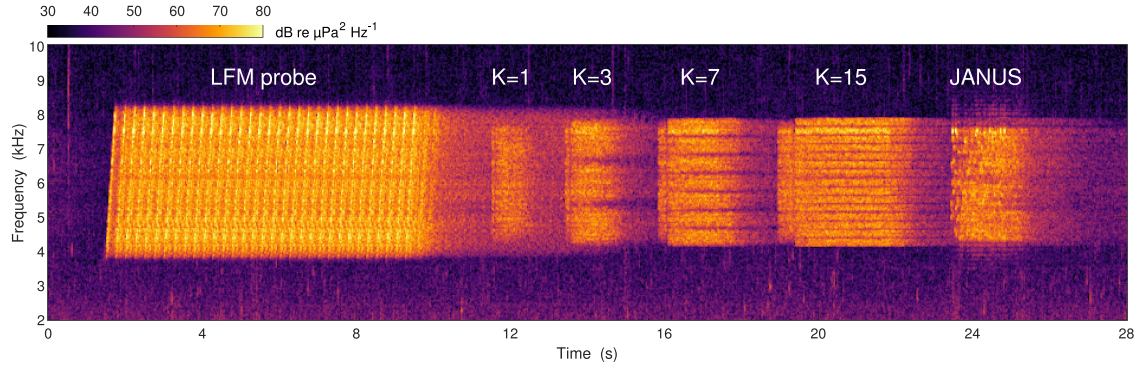

Fig. 3. Spectrogram of the signal sequence received over the link N7→N8, consisting of a channel probe, four FRSS packets, and a JANUS packet. Reverberation is manifest as the diffuse tails of the signals.

unique signaling links. In addition to these horizontal links there are five vertical links, namely from the transmitter to the receiver on the same node. The transmission range is only 5 m and there is some clipping of the data, but nonetheless, it is interesting to verify the prediction methodology for these links.

B. Transmit Schedule

The trial was subdivided into different experiments, with signaling in two frequency bands and with moving and stationary nodes. The present analysis considers one frequency band (4–8 kHz) and the 8 stationary bottom nodes.

Between 18:00 and 20:00 UTC on April 30, five transmitters broadcast a variety of longer (32-s) channel probe signals. These probe signals have different strong and weak points, and yield different measurements errors. The motivation for this experiment was to increase the likelihood of obtaining some high-quality channel measurements for each link. The probe signal that is analyzed in this article is a 250-ms linear frequency modulated (LFM) chirp, repeated eight times at a repetition time of 4 s. This signal is well suited to estimate long delay profiles.

The main experiment of the SALSA trial ran between April 30, 23:00, and May 2, 01:00. The objective of this 26-h experiment was to simultaneously sample the channel and modem performance, over all links and at a high cycle rate. There was only room for a single, short probe signal, consisting of a 250-ms chirp repeated head-to-tail during 8 s. It was followed by a sequence of four frequency-repetition spread spectrum (FRSS) packets with $K \in \{1, 3, 7, 15\}$ subbands, and a JANUS packet: Fig. 3. There is a pause of 2 s between the LFM probe and the $K = 1$ packet, and a pause of 1.5 s between communication packets.

FRSS and JANUS are the physical-layer solutions in SALSA, where JANUS is used for first contact [10]. The JANUS packet is compliant with the standard [14], except for the frequency band, but is not analyzed in this article as the proposed prediction method is applicable only to FRSS. This phase-coherent scheme is described in Section III-C.

The main experiment consisted of 520 cycles at a cycle period of 3 min, where the signal sequence of Fig. 3 was broadcast by the five sender units in a round-robin schedule. N5 transmitted it at 23:00:00 on April 30, N6 at 23:00:30, etc., until the end of the experiment, when N9 transmitted at 00:59:00 on May 2. There were no modem transmissions in the last 30-s time slot of each cycle, rendering it suitable for ambient noise measurements. The data set contains 18 200 unique signal receptions over the 35 horizontal links, or 20 800 receptions if the vertical links are included.

TABLE III
FRSS PARAMETERS

K	R_s (s^{-1})	Filter taps $K \times L$	N_p (chips)	T_tot (s)	R_eff (b/s)
1	2800	1×90	127	0.42	604
3	933	3×30	255	0.86	299
7	400	7×13	511	1.59	161
15	187	15×6	1023	2.97	86

Number of subbands K, symbol rate R_s, number of filter taps, preamble length N_p, total signal duration T_tot, and effective data rate R_eff.

C. Frequency-Repetition Spread Spectrum

This section gives a short summary of the FRSS scheme, referring to the work in [15] for a more detailed description. The FRSS packets consist of a single-carrier *m*-sequence detection preamble, followed by a payload simultaneously modulated onto K subbands. This payload consists of a rate-1/2 convolutionally encoded bit stream, modulated onto quadrature phase-shift keyed (QPSK) data symbols. A sequence of initial training symbols is prepended for equalizer convergence, and the data symbols are interleaved with periodic training symbols. Every third symbol is a training symbol.

A spread-spectrum technique is applied whereby all subbands carry the same symbol stream. This makes the scheme amenable to multiband equalization, featuring joint equalization, and despreading with a theoretical spread-spectrum gain K.

Notice that $K = 1$ is not multiband, but just single-carrier QPSK. Table III summarizes the FRSS packet parameters. Common parameters are a center frequency $f_\mathrm{c} = 6$ kHz and $N_\mathrm{b} = 256$ payload bits. The core of the receiver is a minimum mean-square error (MMSE) linear $K \times L$ multiband equalizer, where L is the number of taps per subband. There are 90 taps in total (91 for $K = 7$), which are updated with the least-mean-squares (LMS) algorithm. Filter coefficients are updated by direct adaptation, using training mode for the training symbols and decision-directed mode for the data symbols. At a fractional tap spacing of $4/(3R_\mathrm{s})$, the delay span is $\Delta\tau = 24$ ms for all K.[2]

[2]The Doppler span in (41) and (42) is not a receiver setting. Predictions based on the delay profile tacitly assume $\Delta v = \infty$, but its actual value is empirically estimated in Section V-G.

The equalizer is centered on the strongest peak of the detector filter output. This centering is a good standard setting, but not necessarily optimal for the communication performance over each link. However, for the performance prediction, it only matters that (38)–(43) agree with the modem implementation.

The equalizer has an integrated phase-locked loop, and the detector uses a bank of Doppler replicas of the *m*-sequence, which yields an estimate of the nominal Doppler shift that is removed by resampling before equalization. Neither of these ingredients is critically important for signaling between stationary bottom nodes, but the modem is run in operational mode for networking scenarios, which also include moving nodes. The analysis shows that the detector occasionally detects a Doppler shift between the bottom units, synchronizing on a sideband in the Doppler spectrum. The length N_{p} of the *m*-sequence detection preamble increases with K to achieve detection at lower input SNR, which is useful because the higher processing gain of a larger K adds robustness to noise and interference. Detection is balanced in that the majority of packets that are not detected, would not have been decoded correctly had they been detected.

The periodic training symbols add robustness and can be used to compute receiver output SNR, recognizing that MMSE equalizers are biased [16]. Experimentally observed bias with practical receiver settings may deviate from the theoretical MMSE bias [17]. When the transmitted symbols are known, like the periodic training symbols of FRSS, the bias can be estimated from the data. Let z_j denote the jth transmitted periodic training symbol, and $\hat{z}_j$ is the received symbol. The equalizer bias estimate is[3]

$$\gamma = \frac{1}{J}\sum_{j=1}^{J} \hat{z}_j z_j^* \tag{53}$$

and the unbiased output SNR computed by the modem is [17]

$$\mathrm{SNR}_{\mathrm{modem}} = \frac{J-1}{J}\frac{\sum_{j=1}^{J}|z_j|^2}{\sum_{j=1}^{J}|z_j - \hat{z}_j/\gamma|^2}\ . \tag{54}$$

Notice that γ corrects the equalizer bias, whereas $(J-1)^{-1}\sum_{j=1}^{J}|z_j - \hat{z}_j/\gamma|^2$ is an unbiased estimate of the "noise" variance. The estimation error $z_j - \hat{z}_j/\gamma$ may have contributions from collisions and the signal's own interference, but this discrimination is reserved for the names of the predicted output SNRs in Section II-B. The measured output SNR is just referred to as $\mathrm{SNR}_{\mathrm{modem}}$.

D. Atomic Clocks

Table II indicates that 7 nodes were equipped with a chip-scale atomic clock. The exception is N4, which is an older design. The advantages of atomic clocks are numerous for uncabled instruments. They permit tight round-robin scheduling over long periods without collisions due to sampling frequency offsets and clock drifts. As the sampling rate of both the transmitter and the receiver are derived from the atomic clock, phase drifts observed in the data are completely due to channel fluctuations or platform motion. The start time of acoustic transmissions is also derived from the atomic clock, which permits monitoring of $\tilde{h}(t,\tau)$ over a long period, and it enables to identify the path the receiver synchronizes on.

E. Channel Sounders

Modem performance is predicted from channel estimates obtained with a correlative chirp sounder. Three sounders are used, with their respective strong and weak points summarized in the following, and further clarified by Table IV and Fig. 4.

1) Sounder 1 is the 250-ms LFM chirp repeated 8 times at a repetition time of 4 s. This sounder does not yield useful information on Doppler spread, but is well suited to estimate delay profiles. The observation window in delay is 4 s, and the atomic clocks permit very accurate stacking of the eight channel snapshots.
2) Sounder 2 uses the first chirp of the 8-s LFM probe from the main experiment, combining all cycles to construct an impulse response matrix measuring $t \times \tau = 26$ h $\times$ 250 ms. There is no Doppler information, and reverberant tails beyond 250 ms are missing from the measurement. The impulse response is not processed further, and is not used for performance prediction. It is only used to show the long-term evolution of the channel.
3) Sounder 3 uses all 32 chirps of the 8-s LFM probe from the main experiment. This permits channel tracking during 8 s, resulting in a delay-Doppler observation window of 250 ms $\times$ 4 Hz. The measurement is available every 3 min during 26 h, for each link, but is more susceptible to systematic measurement errors [18] than the other sounders. Impulse responses longer than 250 ms are aliased in delay, and Doppler shifts outside the range from -2 to $+2$ Hz are aliased in the frequency-shift domain.

The processing is straightforward. The received data are matched-filtered with a zero-Doppler replica chirp, and the resulting channel snapshots are stacked to obtain a discrete-time matrix $\hat{h}(t,\tau)$, which is an estimate of the true matrix $\tilde{h}(t,\tau)$. This matrix has {8, 520, 32} elements in the t dimension for Sounder {1, 2, 3}, respectively. The delay-Doppler spread function (23) is only used with Sounder 3, and is implemented as a 32-point discrete Fourier transform of $\hat{h}(t,\tau)$. The spectrum of the chirps in the transmit wavefiles is flat between 4.25 and 7.75 kHz, which is approximately the band of the communication packets. Beyond these boundaries there is a rapid roll-off, resulting in a close-to-rectangular spectrum. In terms of the frequency response, the matched-filtering is a good approximation of the band-limiting operation (22).

IV. Environment and Channel Characterization

A. Sound-Speed Profiles (SSPs) and Propagation Loss

Fig. 5 shows SSPs measured on three consecutive days. The sound speed in deeper parts of the fjord is fairly stable and only weakly depth dependent, whereas the upper 35 m are governed by strong temperature and salinity gradients. These gradients are due to heating of the upper layer of the water column by the advent of spring, and the inflow of fresh meltwater from the mountains. There is a distinct sound channel, whose axis moves from a depth of 20 m on April 30, to 14 m on May 2. The figure includes markers to indicate the depth of the bottom units.

The SSP and the terrain affect the propagation loss, which is plotted in Fig. 6 for the 35 horizontal links. These measurements use the 8-s LFM probe received on the NILUS top hydrophone. The mean-square sound pressure is converted to a signal level with (5), and the propagation loss follows from (6) and the known source level. The figure includes a reference curve denoting spherical spreading plus absorption

$$\mathrm{PL}_{\mathrm{ref}} = 10\log_{10}\left(\frac{r^2}{r_0^2}\right) + a(f_{\mathrm{c}})r \tag{55}$$

where $a(f)$ is the frequency-dependent absorption coefficient. This coefficient is computed with the empirical formula of Van Moll *et al.* [19], using CTD data for temperature and salinity at a depth of 40 m. This yields $a(f_{\mathrm{c}}) = 0.42$ dB/km.

[3]At a packet size of 256 payload bits, plus 8 flush bits for the convolutional encoder, there are $J = 132$ periodic training symbols.

TABLE IV
SUMMARY OF THE CHANNEL SOUNDERS

Sounder	Waveform	Recurrence	Delay coverage	Doppler coverage	Remark
1	250-ms LFM every 4 s during 32 s.	Every 24 min between April 30, 18:00 and April 30, 20:00.	4000 ms	−0.125 Hz to +0.125 Hz	Ends 3 hours before the main experiment.
2	250-ms LFM.	Every 3 min between April 30, 23:00 and May 2, 01:00.	250 ms	None	No averaging. Not used for prediction.
3	250-ms LFM head to tail during 8 s.	Every 3 min between April 30, 23:00 and May 2, 01:00.	250 ms	−2 Hz to +2 Hz	Possible aliasing in delay and Doppler.

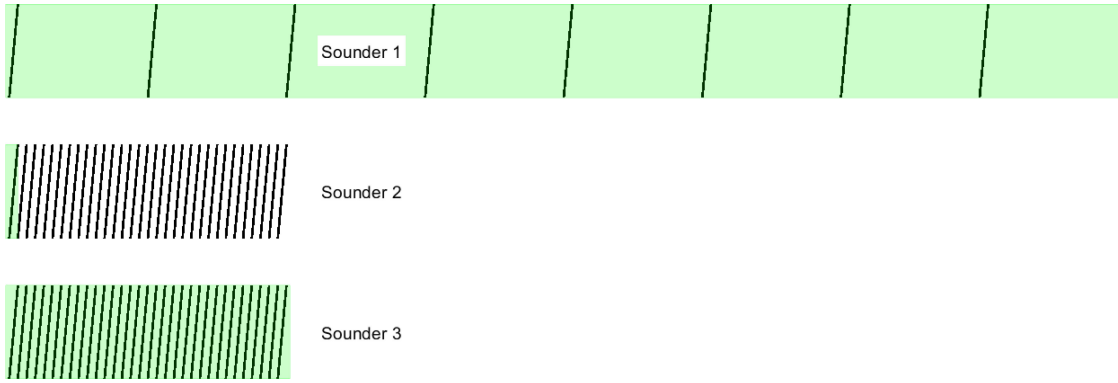

Fig. 4. Sketch of the sounder waveforms. The shaded area is the part of the waveform that is processed.

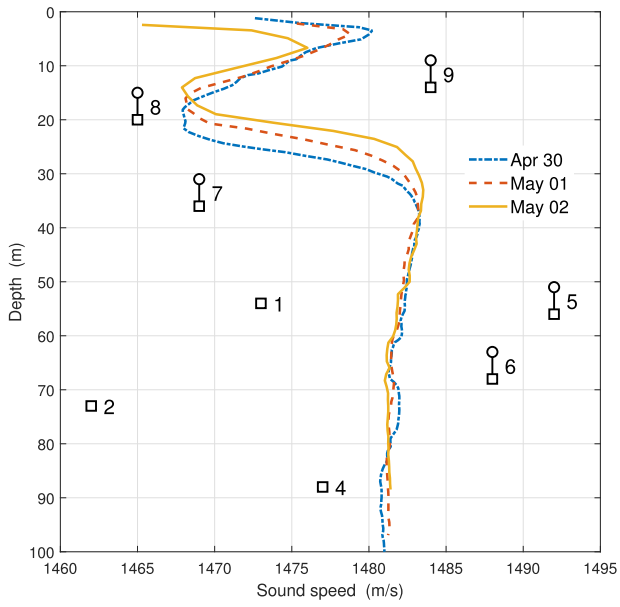

Fig. 5. SSPs measured near N1. The square and round markers indicate the depth of the NILUS receiver and transmitter, respectively. (The horizontal offsets roughly follow a track from northwest to southeast, but internode distances are not to scale.)

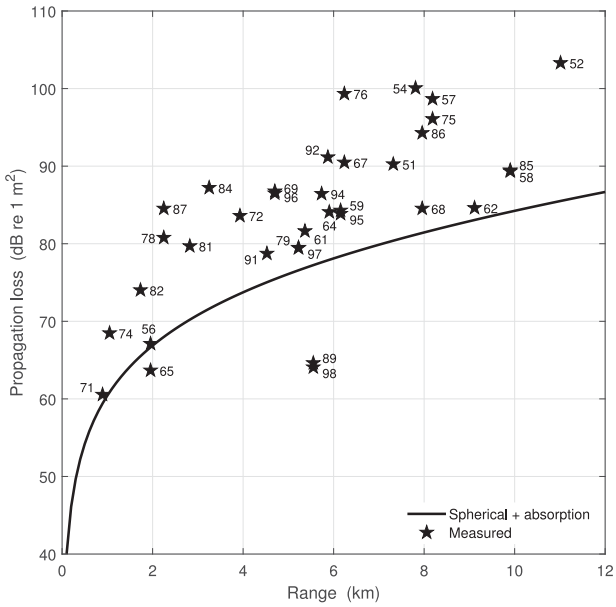

Fig. 6. Measured propagation loss in the 4–8-kHz band. The link N5→N6 is denoted by 56, etc. The loss is averaged over 16 transmission cycles from 00:00 to 00:45 on May 1, which is a period of low ambient noise.

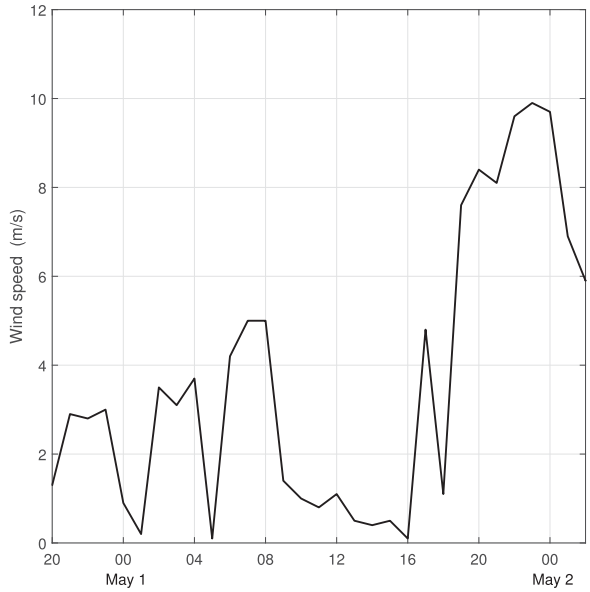

Fig. 7. Wind speed measured by a meteorological station near the trial area.

The bidirectional sound-channel link N8↔N9 is well below the reference curve, and a few short-range links are close. All other links suffer from a propagation loss that exceeds the spherical spreading loss. Some bidirectional links are reciprocal in propagation loss (e.g., N5↔N8, N6↔N9) whereas other ones are not (e.g., N6↔N8, N7↔N8). Ray-tracing with BELLHOP [20] (not shown) reveals that the cause of the high propagation loss is the absence of direct paths. An optical line of sight does not guarantee a line of hearing, and many links depend on surface and bottom bounces to receive signal power.

B. Ambient Noise

The level L_N of the ambient noise was measured in the time slots without modem transmissions, and varied significantly throughout the main experiment. Noise measurements are shown in the analyses in Sections V-E and V-F. The overall picture is one of low ambient noise during the first hours, rising by 20 dB during the day. Superimposed are a series of high-noise events due to nearby ships. May 1 is a national holiday in Norway, and there were many pleasure boats in the area during the day.

C. Wind

Weather information was collected from a meteorological station. The wind speed is plotted in Fig. 7. It increased at 18:00 on May 1, remained high during the evening, and decreased again after midnight. The wind blew from the north during the main experiment.

D. Impulse Response

CIRs are measured with the sounders of Section III-E, which yield the channel $\hat{h}(t,\tau)$ and delay profile $\hat{P}_{\mathrm{d}}(\tau)$, which are estimates of $\tilde{h}(t,\tau)$ and $\tilde{P}(\tau)$. Figs. 8 and 9 show the Sounder-2 impulse response for N5→N6 and N8→N2, which are links that are analyzed in detail in Section V. The atomic clocks give the true propagation delay, and permit the long observation time of 26 h.

Fading is observed for the dominant arrivals at the start of the response. The timescale is too long to associate this fading with Doppler spread, but it does affect modem performance on a packet-by-packet basis. A more striking feature is the dense pattern of weaker arrivals at longer delays. This reverberation carries a nonnegligible fraction of the total signal power, and ultimately limits modem performance. Around 18:00, corresponding with the increase in wind speed, the N8→N2 picture becomes even more diffuse than it already was.

Sounder 2 covers 250 ms in delay, but only $\approx$ 100 ms are shown in Figs. 8 and 9 to highlight the main arrivals. The extent of the reverberation can be studied with Sounder 1. A few characteristic delay profiles are plotted in Fig. 10, including the links N5→N6 and N8→N2. In all cases the strongest arrivals are near the start of the impulse response, and the reverberant tails last for seconds until they reach the noise floor.

E. Collisions and Self-Interference

Fig. 11 illustrates the importance of several terms defined in Section II-B for N7→N8, which is among the most reverberant links. The analysis uses the channel estimate $\hat{h}(t,\tau)$ corresponding to the delay profile (28) shown in Fig. 10. Channel replay [2] is used to separate the useful

$$y_{\mathrm{U}}(t) = \int_{\tau_0-\Delta\tau/2}^{\tau_0+\Delta\tau/2} \hat{h}(t,\tau)\, x(t-\tau)\, \mathrm{d}\tau \tag{56}$$

and the ISI

$$y_{\mathrm{ISI}}(t) = \int_{\tau_{\mathrm{start}}}^{\tau_0-\Delta\tau/2} \hat{h}(t,\tau)\, x(t-\tau)\, \mathrm{d}\tau + \int_{\tau_0+\Delta\tau/2}^{\tau_{\mathrm{start}}+4\,\mathrm{s}} \hat{h}(t,\tau)\, x(t-\tau)\, \mathrm{d}\tau \tag{57}$$

contributions to the total received signal $y(t) = y_{\mathrm{U}}(t) + y_{\mathrm{ISI}}(t)$. The input signal $x(t)$ is the transmit wavefile with the sequence of signals described in Section III-B, shown in Fig. 3 after reception over the same link N7→N8. It is scaled to match the source factor of the experiment, yielding an output signal y in micropascals. The output signal can be retrieved for individual packets by nulling the other packets before the convolution with the channel. Because of estimation errors in the channel response, and because of the time difference between the LFM probe transmission and the FRSS transmissions, the two synthetic components y_{U} and y_{ISI} will not add up precisely to the field observation of y. However, in this simulation, y is also a synthetic signal, equal to the sum of y_{U} and y_{ISI}.

Fig. 11 depicts the resulting situation for $K = 7$, whose useful part is a fairly sharp delineation of the transmitted packet with a detection preamble, short silence, and payload. The ISI part is blurred and continues to increase in intensity until about 1 s into the signal. The total received signal power is the sum of these two contributions. The total power of the $K = 3$ packet is included in the figure. This reverberation tail is approximately 12 dB below the level of y_{U}, whereas y_{ISI} is about 4 dB stronger than y_{U} toward the end of the packet. Self-interference is clearly a bigger concern than reverberation of the previous packet. Even if the equalizer manages to harvest all power of y_{U}, the SIR will not be better than -4 dB plus processing gain.

The terms defined in Section II-B are the steady-state values of the quantities plotted in Fig. 11. $L_{S_{\mathrm{U}}}$ computed from the delay profile with (38) is 94.7 dB, $L_{S_{\mathrm{ISI}}}$ computed with (39) is 98.5 dB, and L_C is about 83 dB re 1 $\mu\mathrm{Pa}^2$. In this type of channel, the mean-square error of the equalized symbols increases again after initial equalizer convergence, because the channel becomes more difficult as reverberation accumulates.

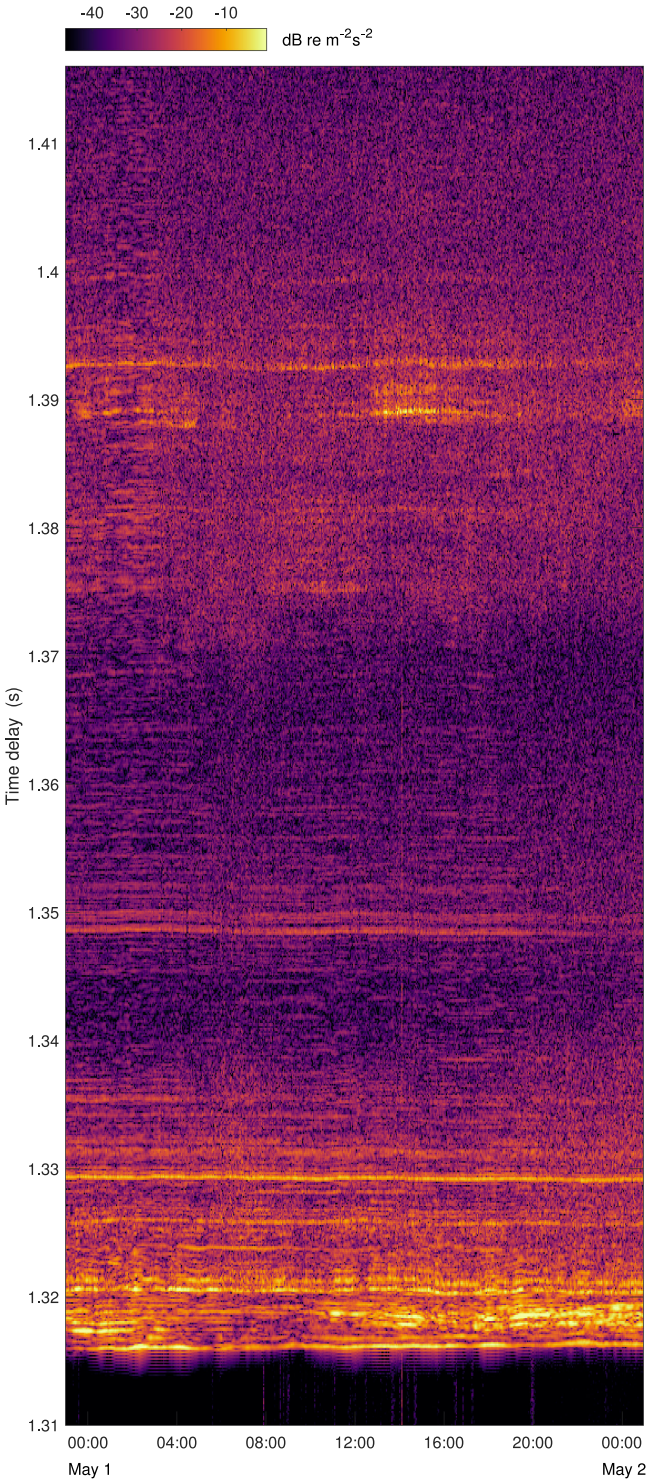

Fig. 8. Long-term channel measurement $10\log_{10}(r_0^2 t_0^2\,|\hat{h}(t,\tau)|^2)$ for the link N5→N6, obtained with Sounder 2, using the reference values $r_0^{-2} = 1\ \mathrm{m}^{-2}$ and $t_0^{-2} = 1\ \mathrm{s}^{-2}$.

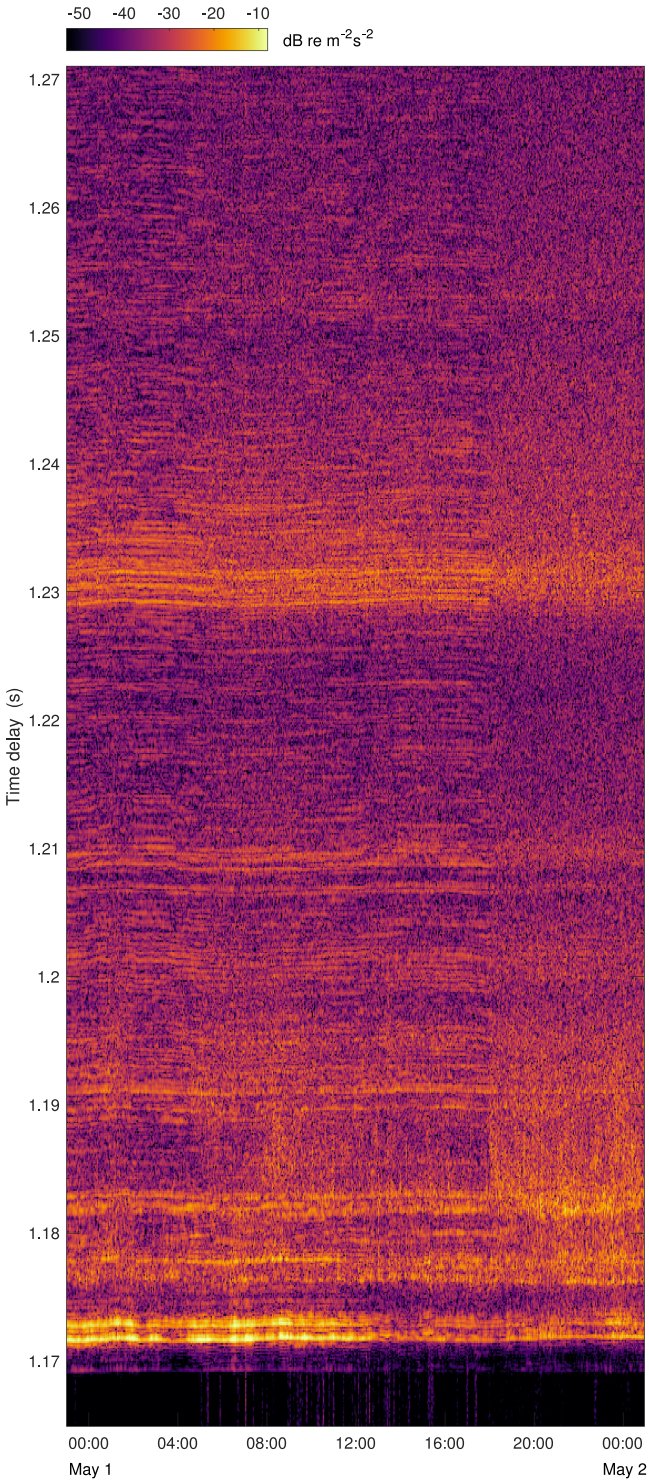

Fig. 9. Long-term channel measurement $10\log_{10}(r_0^2 t_0^2\,|\hat{h}(t,\tau)|^2)$ for the link N8→N2, obtained with Sounder 2.

V. Prediction Results

A. AWGN Channel

Predictions based on the delay profile assume that the equalizer is able to utilize the power of all arrivals within its span, but theoretically an equalizer requires an infinite number of taps to fully equalize even a single path. It is instructive to examine the performance prediction in an AWGN channel, before analyzing the experimental data. To this end, undistorted transmit signals were inserted in a stationary stream of white Gaussian noise, which was fed to the modem software. The input SNR was 10 dB, computed as the ratio of signal power to the expected value of the noise power after filtering the noise stream with the FRSS pulse shape.

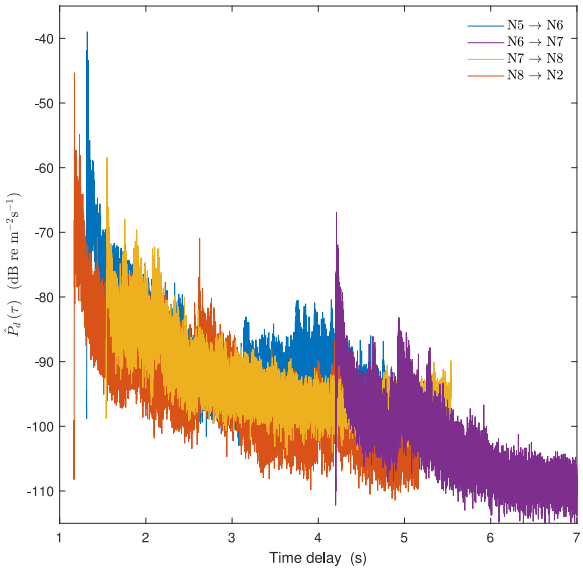

Fig. 10. Examples of power-delay profiles, measured with Sounder 1 between 19:00 and 20:00 on April 30.

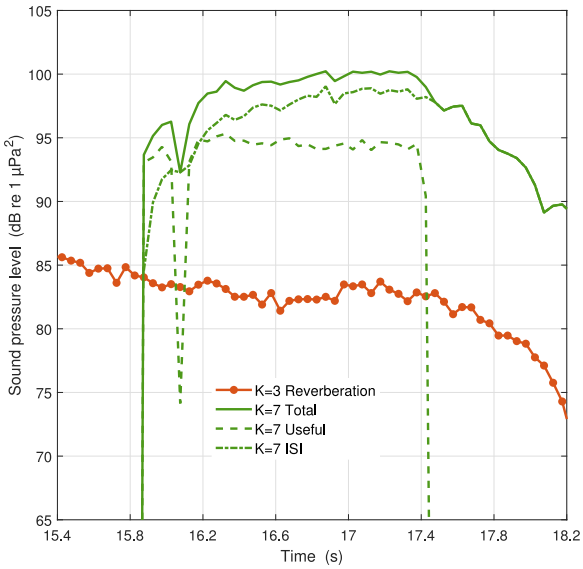

Fig. 11. Levels for a N7→N8 transmission. The time axis is consistent with Fig. 3. An averaging interval of 50 ms is used for the level computation, and $\Delta\tau = 24$ ms.

Fig. 12 shows the modem output SNR for 100 packets. The standard modem settings were used with an LMS step-size parameter $\mu = 0.0033$. The modem output SNR averages about 0.5 dB below the theoretical performance bound (46). It is possible to further approach this bound by reducing μ. This requires a longer training sequence to compensate for the slower equalizer convergence, but doing so, $K = \{1, 3, 7\}$ can be made to average at 0.05 dB below their bounds, and $K = 15$ at 0.15 dB. This demonstrates that the effect of a finite equalizer length is negligible in this regime of output SNR, even for $K = 15$, which has only 6 taps per subband.

However, the main reason for showing these AWGN results is the spread around the mean. A similar variance is observed in the experiment data, and could easily be mistaken for being due to channel fluctuations. The actual cause is the short packet length, with only

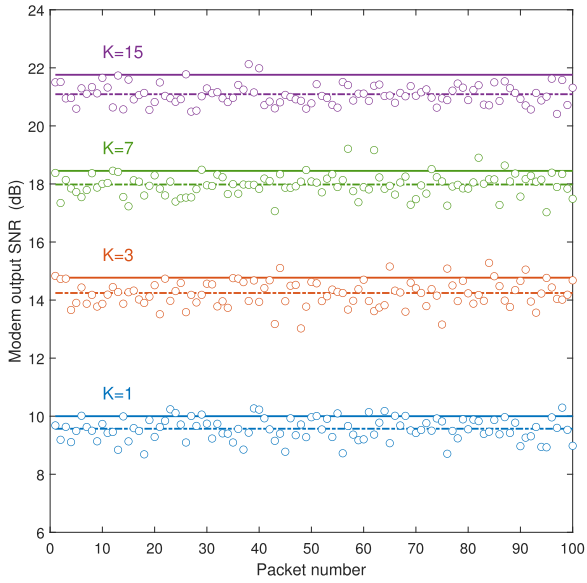

Fig. 12. Modem output SNR for 100 FRSS packets in an AWGN channel with 10-dB input SNR. The solid line is the upper performance bound (46), and the dash-dot line is the mean value of the output SNR.

$J = 132$ periodic training symbols to estimate the output SNR. The integrated noise power fluctuates between packets.

B. Comparison Methodology for the Experimental Data

The analysis consists of two parts. In the first part, the impact of long reverberation tails is examined with Sounder-1 delay profiles. The advantage of Sounder 1 is that high-quality profiles are available for all links, spanning 4 s in delay. From the five transmissions of this signal (see Table IV), the fourth or the fifth one was selected, depending on which one had lower ambient noise at reception.

Modem performance is obtained from the main experiment. A MATLAB version of the modem software was applied to the recorded sea trial data, and the measured output SNR is returned by the receiver as the unbiased estimate (54). Predicted values are obtained with the definitions (46)–(49), where S_{U} and S_{ISI} are computed with (38) and (39). The noise N is measured for each of the 520 cycles, averaging the squared sound pressure over the time slots without modem transmissions. On the other hand, the background $C + N$ in (47) and (49) is measured by averaging over a 100-ms interval just before the arrival of each packet.

There is a latency, because S_{U} and S_{ISI} are measured only once for each link, before April 30, 20:00, whereas the prediction is compared with the modem output SNR from the main run, starting at April 30, 23:00. The SIR prediction (48) is constant, but the SNR, SBR, and SIBR predictions are not constant as N and $C + N$ are updated with each cycle of the main experiment. $C + N$ is measured closer to the packets than N and will contain a more reliable noise estimate under nonstationary noise conditions, but this does not affect the overall picture. The analysis shows that such details are unimportant anyway, as the majority of links are not limited by N or C, but by ISI. Prediction performance is quantified via the prediction error

$$\epsilon = 10 \log_{10} \left(\frac{\mathrm{SNR}_{\mathrm{modem}}}{\mathrm{SNR}} \right) \tag{58}$$

for the SNR hypothesis (46), and similarly for (47), (48), and (49).

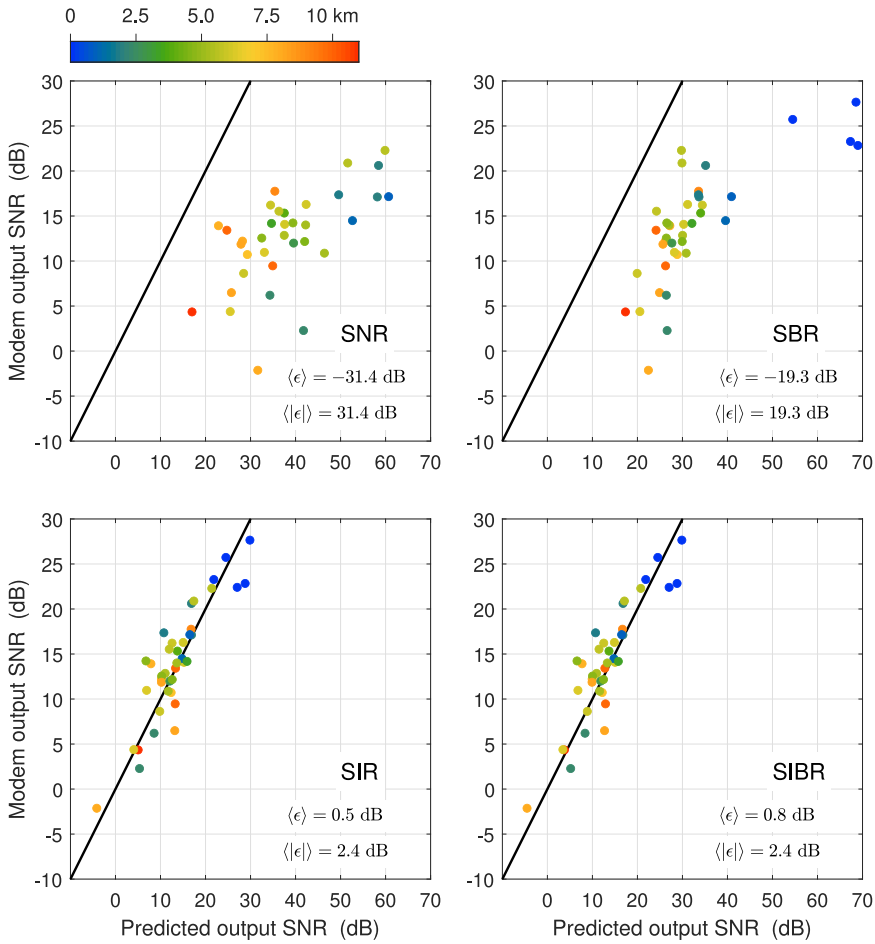

Fig. 13. Sounder-1 prediction results for the $K = 15$ packet transmitted over 35 horizontal links and 5 vertical links, considering transmit cycle 60, between 01:57 and 02:00 on May 1.

The second part of the analysis uses Sounder 3 for the prediction. The delay window is only 250 ms, which limits the applicability to the less reverberant links, but the latency is greatly reduced as S_{U} and S_{ISI} are updated in every cycle. It amounts to about 5–15 s, depending on the FRSS rate; see Fig. 3.

C. Single Transmit Cycle

Fig. 13 visualizes the accuracy of the four hypotheses for the $K = 15$ packets received during a cycle at 02:00 UTC. It is not feasible to label individual links as in Fig. 6, but color coding of the range provides a clue. The panels include $\langle\epsilon\rangle$, which is the prediction error (58) averaged over all links, and also the mean $\langle|\epsilon|\rangle$ of its absolute value.[4]

Clearly, the SNR prediction (46) is far too optimistic about the modem performance. The horizontal links are poorly predicted, and the vertical links are even off the scale. Inclusion of collisions yields a noticeable improvement, as the SBR prediction (47) recognizes that the effective noise background includes reverberation of previous transmissions over the same link. Four vertical links have now entered the scene. However, there is still a sizable gap between measurement and prediction. The SIR prediction (48) does much better with $\langle\epsilon\rangle = 0.5$ dB and $\langle|\epsilon|\rangle = 2.4$ dB, although the error on individual links can still be as large as 7 dB. The SIBR prediction (49) yields no further improvement, confirming that the packet's own reverberation is the predominant performance limiter in this scenario.

The SIBR prediction is of similar fidelity for $K = 3$ and $K = 7$ subbands (not shown) with $\langle\epsilon\rangle = -0.8$ dB and $\langle\epsilon\rangle = -0.2$ dB, respectively. The single-carrier signal is less well predicted with $\langle\epsilon\rangle = -4.2$ dB, but this average is based on fewer links as some packets are not detected.

The main interferer for the vertical links is the surface reflection. The fact that these data are clipped in the recordings does not have a big effect, as QPSK modulation has the information encoded in the phase (zero crossings). Vertical links are, henceforth, omitted from the analysis, which focuses on the more relevant horizontal links.

D. Validity Time of the Prediction

Fig. 13 depicts the prediction performance more than 6 h after the measurement of $\hat{P}_{\mathrm{d}}(\tau)$, but apparently the delay profiles still have reasonable validity. To investigate the validity time, the prediction error is plotted for all 520 cycles in Fig. 14. Each data point represents $\langle|\epsilon|\rangle$ averaged over all available horizontal links. $\mathrm{SNR}_{\mathrm{modem}}$ is not available when a packet is not detected. The $K = 15$ packet is chosen for this analysis because it has the strongest detection preamble. Thirty-one packets are detected on average.

The SNR prediction error varies throughout the experiment, depending on whether there are ships in the area. The prediction performance improves during May 1, when pleasure boats start to dominate the

[4]The notation $\langle\epsilon\rangle$ is used for the link mean to avoid confusion with the temporal mean $\bar{\epsilon}$.

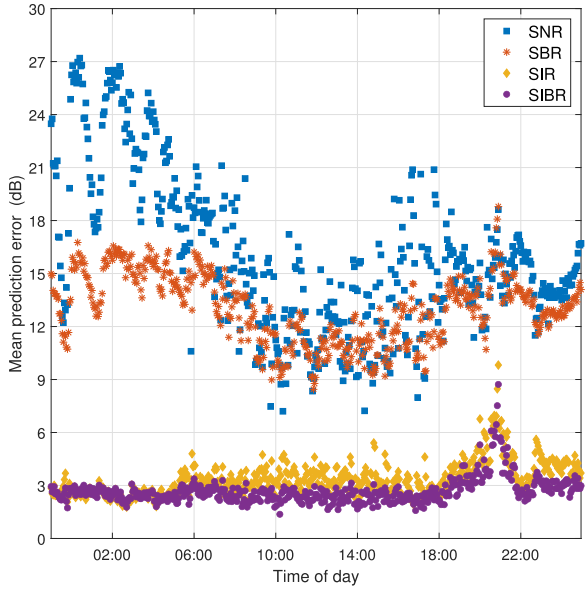

Fig. 14. Mean prediction error $\langle|\epsilon|\rangle$ for the $K = 15$ packet, averaged over up to 35 horizontal links. The prediction is based on Sounder-1 delay profiles.

soundscape, but the mean error is still ≈ 12 dB. It has to be kept in mind that the error is averaged over links with low and high input SNR. The noise is important for some links, but, on average, the SNR prediction is too optimistic even with high shipping activity. The SBR prediction is better than the SNR prediction when the ambient noise is low, but, during the noisy daytime, the difference is small.

The SIR and the SIBR yield a much better prediction. There is virtually no difference between SIR and SIBR during the first 6 h, but as the shipping noise increases on May 1, the SIR prediction deteriorates. The packet's own reverberation is still the most important ingredient, but the prediction can be improved by taking noise into account. Note that the SIR would have deteriorated more if all packets had been detected, because detection failures occur mostly at low input SNR.

The SIBR error is relatively constant until 18:00, but then it increases. The likely cause is the increase in wind speed (see Fig. 7), as data inspection reveals an increase in Doppler spread on several links, where the equalizer is no longer able to harvest all signal power within its span. This will be illustrated in Section V-F.

E. Updating the SIR Prediction

The observation that the mean SI(B)R prediction error is approximately constant until 18:00 in Fig. 14 does not imply that the error is approximately constant over all links. On the contrary, the error fluctuates with time over all links. The data points in Fig. 13 move around between cycles.

Fluctuations are illustrated by examining two links in detail. Differences between the SIR and the SIBR are negligible for these links, and the SIR is used for the prediction as it simplifies the interpretation. An analysis of N5→N6 is presented in Fig. 15, where the top panel displays the signal level (5), the noise level, and the background level. The difference between signal and background is the SBR, which is about 20 dB most of the time, but smaller when there are nearby boats. On average, the SBR is more than sufficient for communication at the modest FRSS data rates. The second panel shows the receiver synchronization, where the atomic clocks permit to pinpoint the arrival time of the path that is centered in the equalizer.

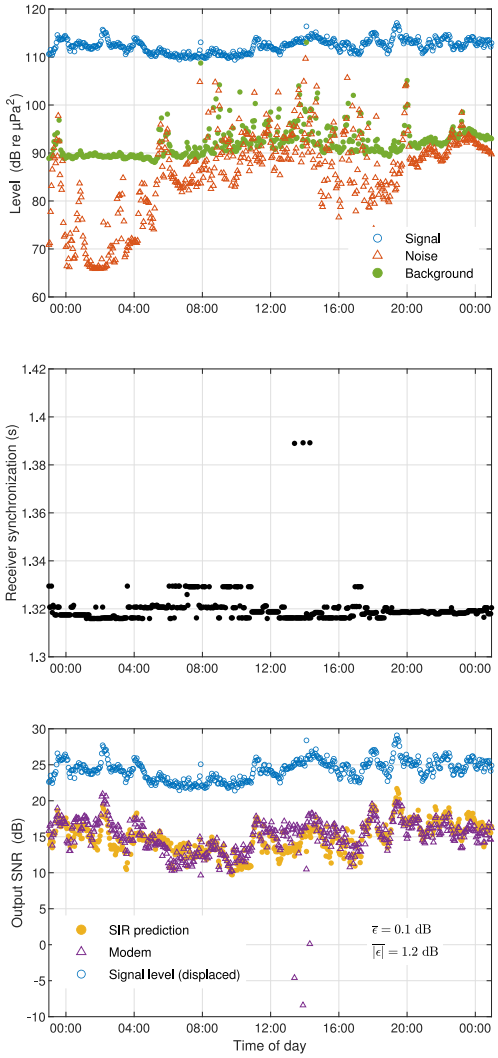

Fig. 15. Detailed $K = 15$ analysis for the link N5→N6. From top to bottom: (a) Signal, noise, and background levels measured in the 4–8-kHz band; (b) receiver synchronization for the $K = 15$ packet; (c) modem output SNR and SIR prediction obtained from Sounder-3 profile updates.

The modem output SNR is plotted in the third panel, together with the Sounder-3 delay-profile SIR prediction for $K = 15$. Sounder 3 has an observation window in delay of only 250 ms, but the N5→N6 profile in Fig. 10 has about 95 % of its power in the first 250 ms, and the resulting measurement error is small. The prediction follows a very similar pattern as the measurement, with $\bar{\epsilon} = 0.1$ dB and $\overline{|\epsilon|} = 1.2$ dB. By contrast, the Sounder-1 SIR prediction for this link is constant at 16.9 dB, and is obviously compromised by channel nonstationarity.

A displaced copy of the signal level reveals a strong correlation with the output SNR. Wind has no noticeable effect on this link, but around 14:00 there are three outliers with a low modem output SNR. The cause of these outliers is revealed by the receiver synchronization. For the three outliers, the detection is at 1.39 s, which is seen to correspond to a delayed arrival in Fig. 8. This arrival competes in strength with the early arrivals around 14:00. Unfortunately this is a poor arrival to synchronize on, as the combined power of the arrivals at the start of the impulse response is much higher. The equalizer has no access to this power, resulting in a low SIR and packet loss. Incidentally, these three packets are the only $K = 15$ packets received with bit errors over this

link. The three outliers are not reproduced by the SIR prediction, and inspection of the corresponding Sounder-3 delay profiles tells that the delayed arrival at 1.39 s is just marginally weaker than the strongest of the early arrivals. This could just be a coincidence due to channel fluctuations, since the prediction is 15 s ahead in time, or a consequence of the normalization algorithm used by the detector. A small change in the channel can have a big effect on modem performance.

F. Doppler Spread

The second link that is scrutinized is N8→N2. Results are shown in Fig. 16, where the first panel gives the signal level, the noise level, and the background level. Sounder 3 was used to estimate the Doppler spectrum, displayed in the second panel. This spectrum is characterized by a peak at zero frequency shift due to stable paths and static scatterers, and sidebands that vary with time.

The third panel compares the modem output SNR and the SIR prediction obtained with Sounder-3 delay profiles. N8→N2 is more reverberant than N5→N6, causing a larger sounding error, but nonetheless the prediction is of similar quality as in Fig. 15—until 18:00. There is a structural decrease in output SNR around 12:00, explained by the fading of the dominant early arrivals visible in Fig. 9. At 18:00, there is a further sudden decrease, where the modem SNR drops by ≈ 9 dB. The prediction fails to reproduce this drop.

Some packets have a very low modem output SNR below -5 dB. This is caused by accumulation of decision errors in the adaptive filtering, derailing the equalizer. The channel becomes too complex to equalize. The signal and background levels do not change at 18:00, but the sudden change coincides with the increase in wind speed (see Fig. 7). This is reflected by the Doppler spectrum, whose sidebands increase abruptly at 18:00, whereas the power density at zero Doppler decreases. Since the signal level remains constant, the effect is due to a redistribution of power in the Doppler domain. The physical mechanisms at play are beyond the scope of this article, but the increased Doppler spread clearly has an effect on the modem performance.

Supporting evidence is obtained by computing the SIR from the Sounder-3 delay-Doppler spread function, using (41) and (42). This requires integration limits for the Doppler domain. The channel tracking capability of $K = 15$ is limited because of its very low symbol rate, and as a first check, the double integral in (41) is evaluated with $2\Delta\upsilon = 0.125$ Hz. This is the Doppler resolution of the measurement, and selects only the zero-Doppler bin for S_{U}. The resulting prediction is plotted in the fourth panel of Fig. 16. It has become more pessimistic before 18:00, where $\overline{\epsilon}$ has increased from 0.7 to 1.6 dB. This suggests that the adopted value of $\Delta\upsilon$ is too small, but, on the other hand, the prediction has improved substantially after 18:00.

The analysis would not be complete without showing the delay-Doppler spread function. Fig. 17 does this for cycles 2 h before, and 2 h after the increase in wind speed. It confirms that the signal power is redistributed in the Doppler domain, and reveals that this occurs at all delays, except for a few arrivals at the start. The green boxes indicate the receiver synchronization for these cycles (for $K = 3$, see Section V-G for the value of $\Delta\upsilon$). The total power within the box is useful in the prediction, and all power outside the box is ISI.

The picture at 20:04:30 is an example where the receiver synchronizes on a sideband in the Doppler spectrum. This happens only sporadically, because the detector filter bank has a spacing of 1 Hz. The receiver can, thus, only synchronize in steps of 1 Hz. The delay-Doppler spread functions in Fig. 17 are computed without resampling of the acoustic data, and the power density at $\upsilon = 0$ Hz is due to static scatterers. Since the preamble detector senses a Doppler shift at 20:04:30, the acoustic data are resampled before the channel equalization. The power in the green box becomes more accessible to the receiver, but the power of the static paths ends up at $\upsilon = -1$ Hz and requires Doppler tracking.

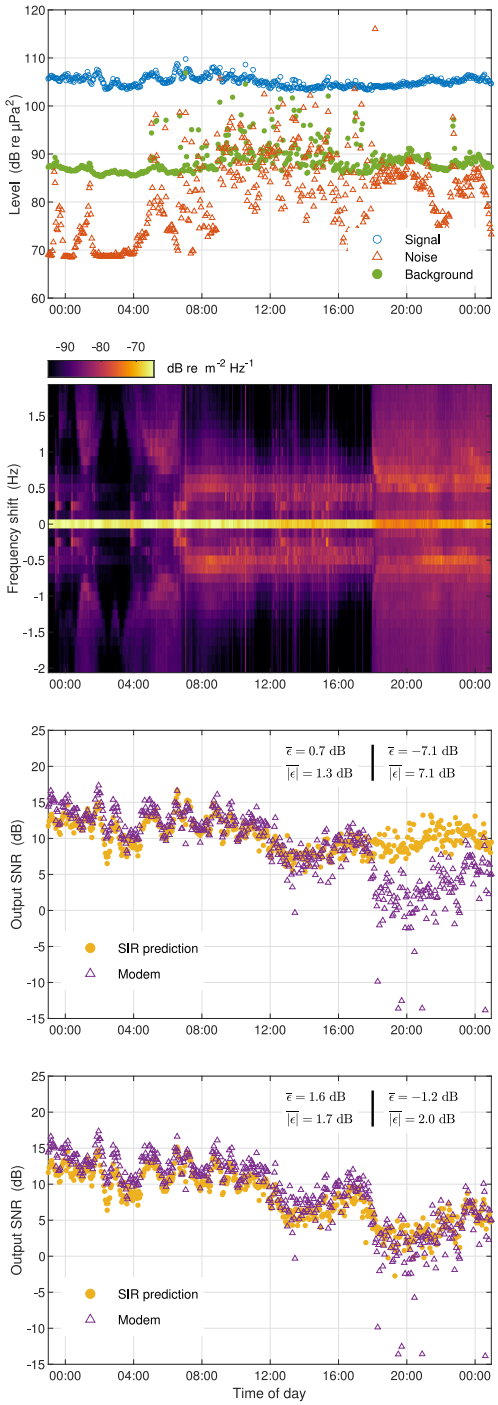

Fig. 16. $K = 15$ analysis for the link N8→N2. From top to bottom: (a) Signal, noise, and background levels measured in the 4–8-kHz band; (b) Doppler power spectrum; (c) modem SNR, and SIR prediction from Sounder-3 profile updates; (d) SIR updates computed from the delay-Doppler spread function. The mean prediction error is given for the signaling interval up to 18:00, and the period after 18:00.

G. Following the Trend

The modem output SNR is characterized by cycle-to-cycle fluctuations superimposed on a more slowly varying trend. To more clearly

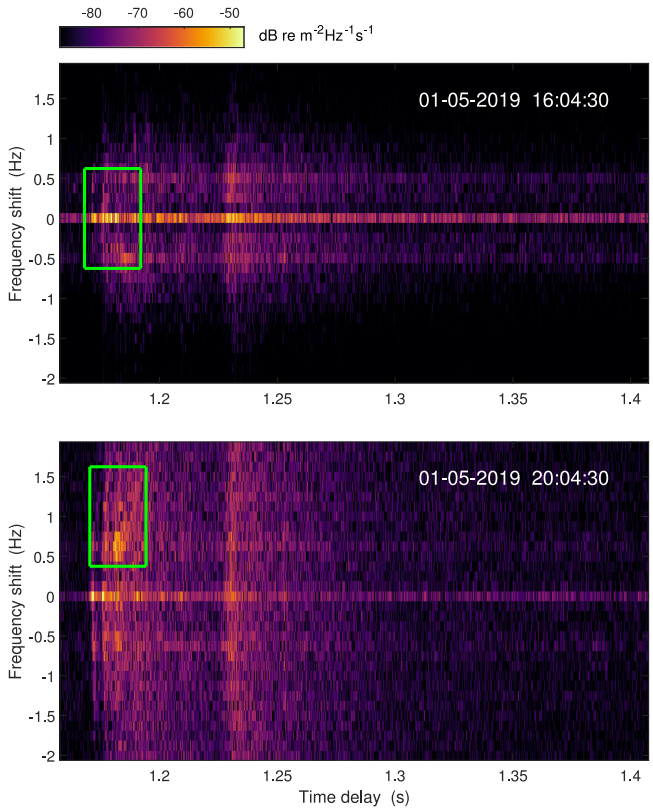

Fig. 17. Delay-Doppler spread function measured over the link N8→N2. The green boxes indicate the area of useful power density, illustrated for $K = 3$. Their horizontal size is $\Delta\tau$, and their vertical size is $2\Delta\upsilon$, in agreement with (41).

examine the prediction of the trend, a 7-point moving average filter is applied to the both the modem output SNR and the prediction. Fig. 18 gives the results for N5→N6, for all FRSS rates, using the SIR computed from the Sounder-3 delay profile. Apart from the distortion around 14:00, due to misprediction of the receiver synchronization, all rates follow the trend well. The three multiband modulations are occasionally somewhat below or above the prediction, but generally have a good match. However, the single-carrier signal is structurally below the prediction.

The moving average filter is applied to N8→N2 in Fig. 19, with a SIR prediction computed from the Sounder-3 delay-Doppler spread function. The receiver is operated differently from Fig. 16, because the weak $K = 1$ detection preamble misses many packets over this link. Missing detections for $K < 15$ are circumvented by enforcing detection on the values of τ_0 and υ_0 obtained with the strong detection preamble of $K = 15$, which is possible thanks to the atomic clocks. Another difference is that the receiver is operated in training mode for all symbols, avoiding decision errors and keeping the equalizer on the rails. For each K, the value of $\Delta\upsilon$ is adjusted to minimize $|\bar{\epsilon}|$ after 18:00.

The $K = 15$ result in Fig. 19 can be directly compared with the fourth panel of Fig. 16, where, apart from the moving-average filter, the only difference is the training mode. This training corrects the outliers below -5 dB and improves other packets as well, increasing the mean modem SNR after 18:00 by 2 dB. Consequently, a larger value of $\Delta\upsilon$ is needed to match prediction and measurement. There is no improvement in modem performance before 18:00, since most decisions were correct already in decision-directed mode. The value of $\Delta\upsilon$ that minimizes the prediction error after 18:00 is included in the figure. It decreases with increasing K, which corroborates the finding in [21] that channel tracking improves with an increasing symbol rate. $K = 15$ still has the highest output SNR after 18:00, but its advantage over the higher rates is smaller than it was before 18:00.

The prediction is remarkably accurate for $K = 3$ throughout the entire experiment, and $\bar{\epsilon}$ is $\{-1.9, -0.2, 0.7, 1.1\}$ dB for $K = \{1, 3, 7, 15\}$, respectively. Sounding errors are unavoidable for this link, since the channel is noticeably overspread after 18:00. It is not possible to separate the contributions of sounding errors and performance modeling errors to the residual prediction error, but sounding errors cannot explain the relative differences between the FRSS rates. Inspection of other links (not shown) reveals that misprediction of the single-carrier signal is a structural problem. The experimentally observed processing gain agrees fairly well with the theoretical gain K throughout the data set, except for $K = 1$. There is, thus, a room for modeling improvement, but the results clearly show the potential of the method.

H. Probability of Bit and Packet Error

Receiver output SNR is an important quality parameter, being more informative about link quality than the SNR at the input of the receiver. However, ultimately the success criteria for digital communication are the BER and the PER, whose expected values are the probabilities of bit and packet error. For Gray-coded QPSK signaling in an AWGN channel, the probability of bit error is given by [22]

$$P_{\mathrm{b}} = \frac{1}{2}\mathrm{erfc}\left(\sqrt{\frac{E_{\mathrm{b}}}{N_0}}\right) \tag{59}$$

where E_{b} is the signal energy per bit, and N_0 is the noise power spectral density. The term "AWGN channel" has the connotation of zero delay-Doppler spread, and/or a perfect receiver that is able to harvest all signal power. P_{b} can be recast in terms of the input SNR as

$$P_{\mathrm{b}} = \frac{1}{2}\mathrm{erfc}\left(\sqrt{\frac{S}{2N}}\right) \tag{60}$$

but the outcome is useless as the channels under consideration are far from AWGN. Instead, it makes much more sense to substitute output SNR. If the real and the imaginary components of the equalized complex QPSK symbols follow a Gaussian distribution, the probability of bit error before the Viterbi decoder is [17]

$$P_{\mathrm{b}} = \frac{1}{2}\mathrm{erfc}\left(\sqrt{\frac{\mathrm{SNR}_{\mathrm{modem}}}{2}}\right). \tag{61}$$

The Gaussian assumption proved a good one for the data examined in [17]. It can be verified for the present data by plotting the BER of the received FRSS packets. A single packet contains only 512 b before the Viterbi decoder, and to improve statistics all detected packets of the 26-h experiment, of all K, are combined in 0.4-dB bins. The bin-averaged P_{b} in Fig. 20 is in good agreement with the theoretical result (61).

The figure includes the probability of packet error after the Viterbi decoder. The authors are not aware of an analytical expression for P_{b} after the Viterbi decoder, but this quantity can be approximated with the "bercoding" function in MATLAB. The red curve is obtained by using the bercoding function to compute P_{b} after the decoder, and the probability of packet error follows as $P_{\mathrm{p}} = 1 - (1 - P_{\mathrm{b}})^{N_{\mathrm{b}}}$, where $N_{\mathrm{b}} = 256$ is the number of information bits. There is a small mismatch between theory and practice, but it is smaller than other uncertainties. It is, thus, possible to convert a delay-Doppler spread function to P_{b} and P_{p}, where the 1–2 dB error in the prediction of output SNR dominates over the error in the conversion to P_{b} and P_{p}.

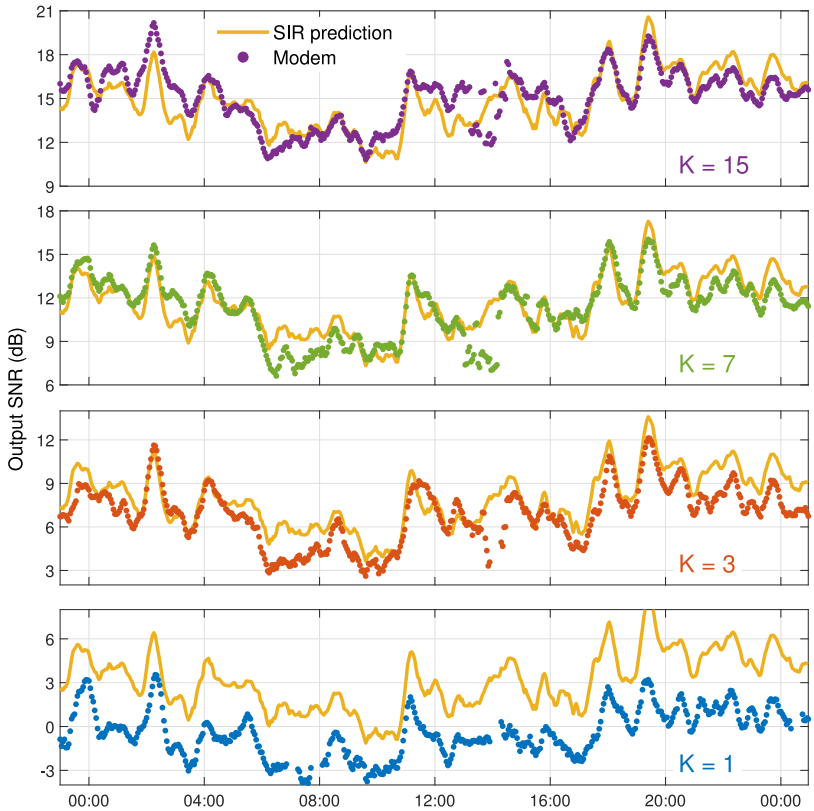

Fig. 18. Comparison of prediction and measurement for N5→N6 for a modem in operational mode. A seven-point moving average filter has been applied to prediction and measurement.

VI. Discussion

The prediction method can be applied to modeled or measured CIRs. Acoustic modeling is not realistic for embedded performance prediction, as acoustic modems do not support full-fledged propagation models, and furthermore, the required environmental input is not available. Moreover, it is challenging enough to model the reverberant tails offline [23]. However, *in situ* performance prediction using measured CIRs is a realistic option. In the network initialization stage, modems could broadcast a probe signal, which is to be processed by receiving modems. These modems can also measure ambient noise and compute the SIBR, to approximately figure out physical layer settings, which meet a given performance requirement.

Prediction (49) is an upper bound if S_{U}, S_{ISI}, N, and C are perfectly known. Yet, Fig. 13 reveals many links whose output SNR exceeds the SIBR prediction. For the most reverberant links, part of the explanation is that S_{U} and S_{ISI} are steady-state values. Fig. 11 illustrates a link where it takes about 1 s for S_{ISI} to reach this value. On average, the packet experiences a higher SIR than the steady-state SIR. Furthermore, $C + N$ is measured just before each packet. Reverberation of previous packets will generally drop during reception of the intended packet. Another possible cause is the frequency dependence of ambient noise and reverberation, which causes the SIBR to vary over the FRSS subbands. The adaptive filter can suppress subbands with a low SIBR, and put a larger weight on subbands with a higher SIBR. However, the most important reason is that the channels are nonstationary. The delay profiles used for the predictions in Fig. 13 were obtained well in advance, and are outdated.

Indeed, the modem output SNR is a function of time, with cycle-to-cycle fluctuations superimposed on a more slowly varying trend. The prediction reproduces the trend and can reach small values of $\bar{\epsilon}$. It also reproduces the spread around the trend, but not the precise fluctuations. Similar fluctuations are observed in the AWGN channel of Section V-A, and these are simply due to the small packet size. Channel variability contributes to the spread, and this can be partly predicted with up-to-date channel information, but there is also an unpredictable component as the receiver synchronization can differ from (40) and (43). The detection preamble senses the channel over a short time and responds to channel fluctuations, even if the channel is stationary between prediction and modem transmission.

A comparison of the modem output SNR between links shows various degrees of covariation. The two analyzed links, N5→N6 and N8→N2, are weakly correlated. Other examples are N8→N4 and N9→N4, which are strongly correlated, and N8→N4 and N8→N9, which are completely uncorrelated. Lack of overall correlation explains why the SIBR prediction error in Fig. 14, which is averaged over all links, is relatively constant over the first 19 h.

Fig. 15 shows an example of a link that is well predicted by the SIR, despite the strong correlation between modem output SNR and the received signal level. At first glance, this correlation might suggest that the output SNR can be further increased by increasing the modem source level, opening up for higher order symbol constellations. However, this is an example of covariation without a causal dependence. The reality is that the link N5→N6 is limited by reverberation at all times. The power S_{ISI} of the reverberant tail is relatively constant, and the fluctuations in signal level are due to fading of the dominant paths near the start of the impulse response (see Fig. 8). These paths are included in S_{U} and are available to the equalizer. Both signal level and SIR covary with S_{U}, and hence, signal level and output SNR are correlated.

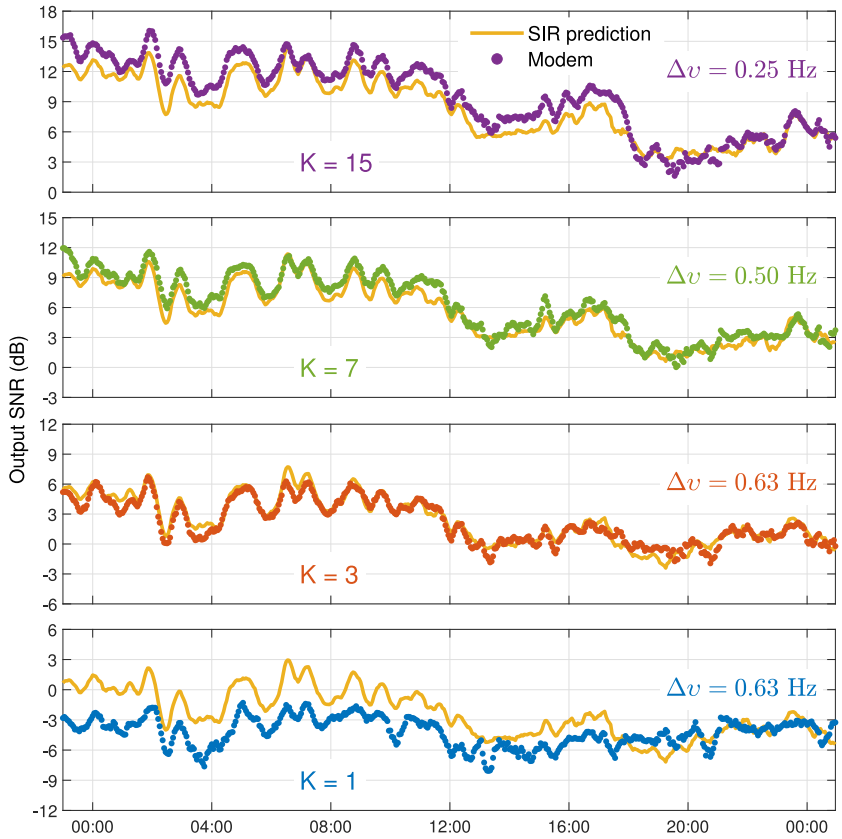

Fig. 19. Comparison of prediction and measurement for N8→N2 with enforced detection and a receiver in training mode. A seven-point moving average filter has been applied to prediction and measurement.

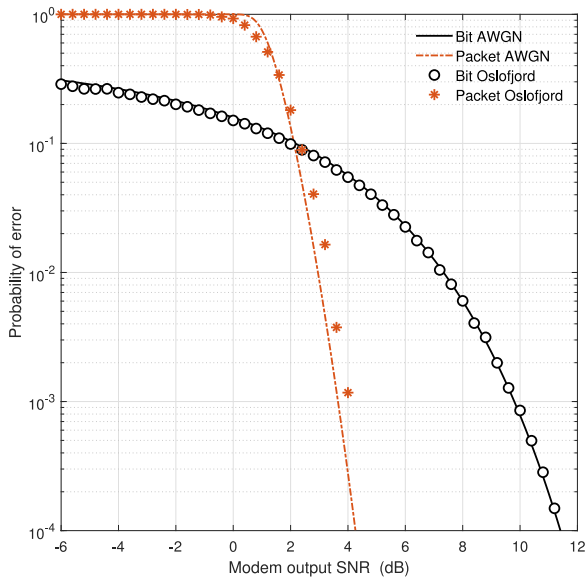

Fig. 20. Probability of bit error before the Viterbi decoder, and probability of packet error after the decoder, from measurement and AWGN theory.

An increase in source level while increasing the signal level does not alter the SIR because it affects S_{U} and S_{ISI} equally. Hence, the modem output SNR will not respond to a higher source level. By adding scaled recorded noise to the data, it is observed that the source level can in fact be reduced by more than 10 dB before the modem output SNR drops by 1 dB.

The objective of this article is to predict modem performance, not to improve it, but there is room for a few observations. Fig. 18 shows compelling evidence that the equalizer is able to constructively combine the power of all available arrivals for this link, except for $K = 1$. Although the FRSS equalizer is a simple, linear equalizer with LMS tap updates, its performance is at the theoretical maximum for the given equalizer length $\Delta\tau$ and synchronization τ_0. Varying $\Delta\tau$ yields some improvement for some links, but the standard modem settings are quite good. $\Delta\tau$ cannot simply be extended to include the reverberant tail, because the excessive number of taps would hinder equalizer convergence. Sparse channel equalization techniques, e.g., [24], have recently been proposed for channels where most of the power is localized around several small regions in delay and Doppler. The potential of sparse channel equalization is small for the densely populated Oslofjord channels. The recursive least squares (RLS) tap update yields some improvement for $K = 1$ over some links, but the other rates actually perform worse with RLS. Addition of a feedback section also improves $K = 1$ over some links, but does not yield a structural improvement for this data set.

There is some Doppler spread during the first 19 h of the experiment, but it does not noticeably affect modem performance. When the wind picks up the Doppler spread increases considerably on several links, where the equalizer is no longer able to harvest all power within its span. The single-carrier signal is least affected, and the $K = 15$ signal is most affected by the wind. This can be explained by their symbol rates, as a higher symbol rate results in better tracking of channel fluctuations [21]. Fig. 19 illustrates that a prediction based on the delay-Doppler spread

function can successfully handle scenarios with a large Doppler spread.

The single-carrier signal is least well predicted throughout the data set, with a modem SNR that is several decibels below the prediction. This appears to be due to the fact that the equalizer operates in a regime of low output SNR, where it fails to converge to the MMSE solution. The same deviation is observed in the AWGN channel of Section V-A if the input SNR is reduced, even with an equalizer in training mode. This behavior of the adaptive filter and the effect of decision errors have to be included in the modeling to improve the prediction at low output SNR. The value of Δv, manually tuned in Fig. 19, might also be derived from adaptive-filter theory.

The collisions considered in this article are soft collisions due to reverberation of previous packets transmitted over the same link. The spacing between successive signals (see Fig. 3) is a compromise between minimizing interference between packets, and maximizing the cycle rate of the experiment. Despite the visible leakage of one signal into the next one in Fig. 3, a larger spacing would hardly improve communication performance. The analysis shows that the interference by previous packets is much smaller than the packet's own interference. Similar arguments can be used for the spacing between detection preamble and payload. From the perspective of raw modem performance and efficiency, it makes no sense to make it larger than the equalizer length. Beyond this length, reverberation of the preamble into the payload is less harmful than reverberation of the payload into itself. Any saving in packet length is beneficial for network performance, as it decreases the probability of collision between different links.

Although the soft collisions of the present experiment were not very harmful, actual network collisions are not necessarily soft. C in (47) and (49) may become a performance-limiting factor in the presence of hard collisions between packets transmitted by different senders. The predictions assume that all terms in the denominator of (47) and (49) are mean-square sound pressure contributions, which act as noise. A special situation arises when the collision is between like packets, e.g., two $K = 15$ packets, using the same sequence of training symbols. In that case, the colliding packet is correlated with the intended packet, and the outcome becomes less predictable. Colliding signals of other modulation types are covered by the prediction method, so long as they are wideband modulations in the same frequency band. Colliding signals or noise sources with a very different spectral distribution, such as narrowband noise, are not covered by the method in its present form.

On average, ambient noise was less important than a packet's own reverberation, despite a propagation loss that exceeds the spherical spreading loss over most links, and despite a 20-dB increase in noise level during daytime on May 1. The packet's own reverberation is the dominant factor that limits modem performance in this environment. The difference in modem depths, combined with the SSP, cause the propagation loss and the severity of the reverberation to be a function of link rather than range. Practical spreading laws [25] cannot be used to approximate the propagation loss, and some links over long ranges are much easier than other ones over short ranges, and *vice versa*. This is further investigated in the SALSA project, where the sea trial data are used for research on smart adaptive networking.

VII. Conclusion

Measurements of the time-varying impulse response have been calibrated for the propagation loss, bridging the gap between underwater acoustics and communication channel terminology. Calibrated CIRs were used to predict the output SNR of a phase-coherent acoustic modem equipped with an adaptive channel equalizer. The key assumption of the prediction method is that the received power distribution in delay and Doppler can be subdivided into a region that is accessible to the equalizer, and an inaccessible region. Knowledge of only the power-delay profile is sufficient under calm conditions, with the prediction being in good agreement with measurements over 35 horizontal links and 5 vertical links. As the Doppler spread increases, the delay profile no longer provides sufficient information, and the prediction instead has to consider the delay-Doppler spread function.

For subband modulation, the prediction was accurate within 1–2 dB if the channel information was up to date. This is surprisingly good given the relative simplicity of the methodology. The prediction error was larger for the single-carrier signal. The method is applicable to a single-hydrophone receiver, which is what most acoustic modems use, and should be extensible to other coherent schemes using a channel equalizer. It can be used with modeled or measured CIRs, whose accuracy is critical to the fidelity of the prediction. For the present data set, it was often impossible to tell whether the residual prediction error was mostly caused by channel measurement errors, or by deficiencies of the prediction method and its underlying assumptions.

Acknowledgment

Credits are due to the numerous people who contributed to the sea trial. Special thanks to Joachim Eastwood for enabling the atomic-clock synchronization.

References

[1] M. E. G. D. Colin, R. Otnes, P. A. van Walree, M. K. Prior, H. S. Dol, and M. A. Ainslie, "From sonar performance modelling to underwater communication performance modelling," in *Proc. 4th Underwater Acoust. Conf. Exhib.*, 2017, pp. 221–228.

[2] P. A. van Walree, F.-X. Socheleau, R. Otnes, and T. Jenserud, "The watermark benchmark for underwater acoustic modulation schemes," *IEEE J. Ocean. Eng.*, vol. 42, no. 4, pp. 1007–1018, Oct. 2017.

[3] M. Siderius, M. B. Porter, P. Hursky, V. McDonald, and the KauaiEx Group, "Effects of ocean thermocline variability on noncoherent underwater acoustic communications," *J. Acoust. Soc. Amer.*, vol. 121, no. 4, pp. 1895–1908, Apr. 2007.

[4] I. Karasalo, T. Öberg, B. Nilsson, and S. Ivansson, "A single-carrier turbo-coded system for underwater communications," *IEEE J. Ocean. Eng.*, vol. 38, no. 4, pp. 666–677, Oct. 2013.

[5] J. C. Preisig, "Performance analysis of adaptive equalization for coherent acoustic communications in the time-varying ocean environment," *J. Acoust. Soc. Amer.*, vol. 118, no. 1, pp. 263–278, Jun. 2005.

[6] W.-B. Yang and T. C. Yang, "M-ary frequency shift keying communications over an underwater acoustic channel: Performance comparison of data with models," *J. Acoust. Soc. Amer.*, vol. 120, no. 5, pp. 2694–2701, Oct. 2006.

[7] M. Stojanovic, "Retrofocusing techniques for high rate acoustic communications," *J. Acoust. Soc. Amer.*, vol. 117, no. 3, pp. 1173–1185, Mar. 2005.

[8] H. C. Song, W. S. Hodgkiss, and S.-M. Kim, "Performance prediction of passive time reversal communications (L)," *J. Acoust. Soc. Amer.*, vol. 122, no. 5, pp. 2517–2518, Jan. 2008.

[9] D. A. Abraham and A. P. Lyons, "Novel physical interpretations of K-distributed reverberation," *IEEE J. Ocean. Eng.*, vol. 27, no. 4, pp. 800–813, Oct. 2002.

[10] H. Dol, "EDA-SALSA: Towards smart adaptive underwater acoustic networking," in *Proc. OCEANS Conf.*, Marseille, France, Jun. 2019, pp. 1–6.

[11] *Underwater Acoustics - Terminology*, ISO 18405:2017(E), International Organization for Standardization, Geneva, Switzerland, Apr. 2017.

[12] P. A. Bello, "Characterization of randomly time-variant linear channels," *IEEE Trans. Commun. Syst.*, vol. CS-11, no. 4, pp. 360–393, Dec. 1963.

[13] H. S. Dol, P. Casari, T. van der Zwan, and R. Otnes, "Software-defined underwater acoustic modems: Historical review and the NILUS approach," *IEEE J. Ocean. Eng.*, vol. 42, no. 3, pp. 722–737, Jul. 2017.

[14] J. Potter, J. Alves, D. Green, G. Zappa, I. Nissen, and K. McCoy, "The JANUS underwater communications standard," in *Proc. IEEE Underwater Commun. Netw.*, Sep. 3–5, 2014, pp. 1–4.

[15] R. Otnes, P. A. van Walree, H. Buen, and H. Song, "Underwater acoustic network simulation with lookup tables from physical-layer replay," *IEEE J. Ocean. Eng.*, vol. 40, no. 4, pp. 822–840, Oct. 2015.
[16] J. M. Cioffi, G. P. Dudevoir, M. V. Eyuboglu, and G. D. Forney, "MMSE decision-feedback equalizers and coding—Part I: Equalization results," *IEEE Trans. Commun.*, vol. 43, no. 10, pp. 2582–2594, Oct. 1995.
[17] P. van Walree, "On the definition of receiver output SNR and the probability of bit error," in *Proc. MTS/IEEE OCEANS Conf.*, Bergen, Norway, Jun. 2013, pp. 1–9.
[18] G. Matz, A. F. Molisch, F. Hlawatsch, M. Steinbauer, and I. Gaspard, "On the systematic measurement errors of correlative mobile radio channel sounders," *IEEE Trans. Commun.*, vol. 50, no. 5, pp. 808–821, May 2002.
[19] C. A. M. van Moll, M. A. Ainslie, and R. van Vossen, "A simple and accurate formula for the absorption of sound in seawater," *IEEE J. Ocean. Eng.*, vol. 34, no. 4, pp. 610–616, Oct. 2009.
[20] M. B. Porter, "The BELLHOP Manual and User's Guide: Preliminary Draft (2011)." Accessed: Jan. 20, 2012. [Online]. Available: http://oalib.hlsresearch.com/Rays/HLS-2010-1.pdf
[21] M. Stojanovic, J. G. Proakis, and J. A. Catipovic, "Performance of high-rate adaptive equalization on a shallow water acoustic channel," *J. Acoust. Soc. Amer.*, vol. 100, no. 4, pp. 2213–2219, Oct. 1996.
[22] J. G. Proakis and M. Salehi, *Digital Commun.*, 5th ed. New York, NY, USA: McGraw-Hill, 2008.
[23] T. Jenserud and S. Ivansson, "Measurements and modeling of effects of out-of-plane reverberation on the power delay profile for underwater acoustic channels," *IEEE J. Ocean. Eng.*, vol. 40, no. 4, pp. 807–821, Oct. 2015.
[24] W. Li and J. C. Preisig, "Estimation of rapidly time-varying sparse channels," *IEEE J. Ocean. Eng.*, vol. 32, no. 4, pp. 927–939, Oct. 2007.
[25] M. A. Ainslie, P. H. Dahl, C. A. F. de Jong, and R. M. Laws, "Practical spreading laws: The snakes and ladders of shallow water acoustics," in *Proc. 2nd Int. Conf. Exhib. Underwater Acoust.*, Jun. 2014, pp. 22–27.

Paul A. van Walree (Member, IEEE) received the M.Sc. and Ph.D. degrees in solid-state physics from Utrecht University, Utrecht, The Netherlands, in 1992 and 1997, respectively.

From 1998 to 2009, he was an Underwater Acoustician with the Netherlands Organisation for Applied Scientific Research (TNO), The Hague, The Netherlands. In 2009, he started as a Research Scientist with the Maritime Systems Department, Norwegian Defence Research Establishment (FFI), Horten, Norway. His research interests include acoustic communication, channel characterization and simulation, and miscellaneous topics in underwater acoustics and sonar.

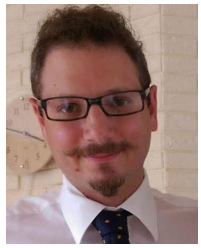

Mathieu E. G. D. Colin received the M.Sc. degree in electronic engineering from the Ecole Nationale Superieure des Ingénieurs des Etudes et Techniques de l'Armement (ENSIETA), Brest, France, in 2001, and the Ph.D. degree in underwater acoustics from the Faculty of Aerospace Engineering, Delft University of Technology, Delft, The Netherlands.

Since 2001, he has been with the Sonar Department, The Netherlands Organisation for Applied Scientific Research (TNO), The Hague, The Netherlands, working on sonar-related topics, such as performance modeling and signal processing.